Multi-scale modeling and analysis of an industrial HVOF thermal spray process

Mingheng Li, Panagiotis D. Christofides*

Department of Chemical Engineering, University of California, 405 Hilgard Avenue, Box 951592, Los Angeles, CA 90095-1592, USA

Abstract

A hybrid (deterministic/stochastic) fundamental model is proposed for the major physico-chemical processes involved in an industrial HVOF thermal spray process (Diamond Jet hybrid gun, Sulzer Metco, Westbury, NY, USA). The model includes continuum type differential equations that describe the evolution of gas and particle temperature and velocity, and a rule-based stochastic simulator that predicts the evolution of the coating microstructure. Regarding gas/particle dynamics, the Reynolds- and Favre-averaged Navier–Stokes equations and the energy balance equations are solved with the renormalization group (RNG) k–ε turbulence model, and the particle trajectories, temperature histories and melting degrees are determined using the fourth-order Runge–Kutta method. On the microscopic particle deposition process, the formation of coating microstructure is captured by the Madejski deformation model and several rules that govern splat formation, solidification and coating growth. Based on the proposed model, a detailed comprehensive parametric analysis is carried out to study the relationship between the key process parameters and the particle in-flight behavior as well as the resulting coating properties.
© 2005 Elsevier Ltd. All rights reserved.

Keywords: HVOF thermal spray; Coating microstructure; CFD; Modeling; Analysis

1. Introduction

Currently, there is a great interest in the field of nanostructured (also called nanoscale, nanophase or nanocrystalline) materials, whose grain sizes are typically less than 100 nm (Cheng et al., 2003). This interest is motivated by the discovery that such materials have properties superior to those of conventional bulk materials including greater strength, hardness, ductility and sinterability, size-dependent light absorption, and reactivity. With the recent advances in the production of high quality nanoscale powders, including atomization, colloidal precipitation, mechanical milling, and vapor phase nucleation and growth (see, for example, Mueller et al., 2003, 2004; Wegner and Pratsinis, 2003; Xun et al., 2004), the focus of nanostructured materials research is now shifting from synthesis to processing, for example, the fabrication of nanostructured coatings using the high velocity oxygen-fuel (HVOF) thermal spray process (He et al., 2000; Ajdelsztajn et al., 2002). The nanostructured coatings are extensively tested in many industries as thermal-barrier and wear-resistant surface layers to extend product life, increase performance and reduce production and maintenance costs.

The physical and mechanical properties of HVOF sprayed coatings are strongly influenced by the nano- or microstructure of the deposit, which, in turn, depends to a large extent on the physical and chemical states of particles at the point of impact on the substrate, such as velocity, temperature, degree of melting and oxidant content. These variables, however, are strongly dependent on several key process parameters including the fuel/oxygen ratio, total gas flow rate, spray distance and powder size distribution (Li et al., 2004b). In order to improve coating performance, much experimental work has been done in the last decade to study the effect of these key process parameters on the physical

and mechanical properties of HVOF sprayed coatings (e.g., de Villiers Lovelock et al., 1998; Lugscheider et al., 1998; Gourlaouen et al., 2000; Hearley et al., 2000; Lih et al., 2000; Gil and Staia, 2002). The optimization of process parameters involved in these works usually relies on cost intensive trial and error procedures, for example, the conventional Taguchi method, which uses a set of orthogonal arrays that stipulates the way of conducting the minimal number of experiments that could give the full information of all the factors affecting the coating performance parameters (de Villiers Lovelock et al., 1998). This approach is expensive but reliable for a specific HVOF thermal spray process. However, a lack of fundamental understanding of the dynamics of the gas and particle behavior as well as of the microscopic deposition process significantly restricts its applicability because the experimentally derived "optimal" solution is not directly applicable to other thermal spray processes in which some important parameters, such as nozzle configuration, powder or fuel type, etc., are different (Cheng et al., 2003). It is in this context that the computational fluid dynamics (CFD) analysis of gas dynamics and particle in-flight behavior in HVOF thermal spray systems is of great importance. Coordination between theoretical CFD modeling and experimental efforts is expected to be mutually beneficial for both investigations.

The HVOF thermal spray process is very complex regarding description in a theoretical model, because it involves combustion, turbulence, compressible flow, multiphase interactions, subsonic/supersonic transitions and droplet deformation and solidification. There are four main physico-chemical processes occurring in the thermal field and flow field: transformation of chemical energy into thermal energy of the gas by fuel combustion, conversion of thermal energy into kinetic energy of the gas jet by expansion through the nozzle, transfer of momentum and heat from the gas to the powder particles, and conversion of particle kinetic and thermal energy into internal energy at coating deposition. It is widely acknowledged that the higher the particle velocity, the denser the coating (Cheng et al., 2001b). In order to transfer as much kinetic energy as possible to the particles, the gas jet is typically maintained at supersonic conditions outside of the torch. This is realized by a convergent–divergent nozzle (Cheng et al., 2003). As long as a sufficiently large nozzle pressure ratio (NPR) is maintained, the gas will be accelerated to achieve sonic velocity at the throat of the nozzle and supersonic velocity in the divergent section. However, depending on the values of the pressure at the gun exit and ambient pressure, the flow condition at the exit of the gun may be under-expanded ($P_e > P_a$), ideally expanded ($P_e = P_a$) or over-expanded ($P_e < P_a$). The Diamond Jet hybrid HVOF thermal spray process (Sulzer Metco, Westbury, NY, USA), which is of interest in this work, is designed to have over-expanded flow conditions at the exit of the torch in order to achieve a higher gas velocity (Mills, 2003). In the past

decade, extensive CFD work has been done to obtain an in-depth understanding of the physio-chemical behavior involved in various HVOF thermal spray processes (Power et al., 1991; Chang and Moore, 1995; Oberkampf and Talpallikar, 1996; Yang and Eidelman, 1996; Hassan et al., 1998; Lopez et al., 1998; Gu et al., 2001; Cheng et al., 2001b; Dolatabadi et al., 2003). However, most of HVOF systems in these studies have underexpanded flow conditions. Moreover, the particle melting behavior, which plays a very important role in the formation of the coating microstructure (Li et al., 2004b; Shi et al., 2004), has never been studied by existing CFD investigations. Finally, multi-scale modeling of the HVOF thermal spray process, which includes the macroscopic two-phase flow and the microscopic particle deposition process, has not been addressed in the existing literature.

In a previous work (Li et al., 2004b), a comprehensive control-relevant parametric analysis of the industrial Diamond Jet hybrid HVOF thermal spray using a simplified one-dimensional model was performed and a feedback control system targeting the control of volume-based average of particle velocity and melting degree at the point of impact on the substrate by manipulating the feeding gas flow rates was proposed. In this work, we focus on multi-scale modeling and analysis of gas dynamics, particle in-flight behavior and coating microstructure evolution in the industrial Diamond Jet hybrid HVOF thermal spray process, using a comprehensive model. The thermal and flow fields of the gas are solved by Eulerian approach and the particle velocity, temperature and degree of melting by Lagrangian approach. On the gas dynamics side, we solve the Reynolds and Favre-averaged Navier–Stokes equations. Due to high Reynolds numbers and large pressure gradients in the nozzle, the renormalization group (RNG) k–ε turbulence model is used with the non-equilibrium wall function treatment to enhance the prediction of the wall shear and heat transfer. The eddy dissipation model, which assumes that the reaction rate is limited by the turbulent mixing rate, is employed to model the chemistry. The governing mass, momentum and energy balance equations together with the ideal gas state equation are solved at first using a first-order upwind scheme to get to a convergent solution and then a second-order upwind scheme to capture the shock diamonds that occur in the external flow field. On the particle dynamics side, we solve the equations that describe the particle trajectories, temperature histories and melting degrees using the fourth-order Runge–Kutta method. The formation of coating microstructure is modelled by stochastic simulation, in which certain basic rules are applied to encapsulate the main physical features involved in the deposition process. Based on the proposed model, a detailed comprehensive parametric analysis is carried out to study the relationship between the key process parameters and the particle in-flight behavior as well as the resulting coating properties.

2. Fluid dynamics

2.1. Torch design

Fig. 1 shows a schematic diagram of the Diamond Jet hybrid gun. The fuel gases (typically propylene or hydrogen), which are thoroughly mixed with oxygen through a siphon system, are fed to the air cap, where they react to produce high temperature combustion gases. The exhaust gases, together with the air injected from the annular inlet orifice, expand through the nozzle to reach supersonic velocity. The air cap is cooled by both water and air ("hybrid") to prevent from being melted. The powder particles are injected at the central inlet nozzle using nitrogen as the carrier gas. Consequently, rapid momentum and heat transfer between the gas and the powder particles lead to acceleration and heating of the particles. The molten or semi-molten particles are carried towards the substrate by the expanding gas jet. The particles hit the substrate, cool and solidify, forming a thin layer of coating material with low porosity. The HVOF thermal spray process is characterized by very high gas and particle velocities and relatively low gas and particle temperatures, as compared to plasma spray processes. Therefore, the HVOF technique is especially suitable for the fabrication of nanostructured coatings. The high particle velocity leads to densification of the coating and the short residence time in the relatively low temperature gas flame makes the powder particles highly plastic and superheating or vaporization is prevented.

2.2. Governing equations

In the macroscopic HVOF flow field, the three major physico-chemical processes (transformation of chemical energy into thermal energy by the combustion of the fuel, conversion of thermal energy into kinetic energy of the burning gases by passing through the nozzle, and transfer of momentum and heat from the gases to the powder particles) are actually coupled together. To simplify the analysis, the process model used in this paper is based on the one-way coupling assumption, i.e., the existence of particles has a minimal influence on the gas dynamics while the particle in-flight behavior is dependent on the gas thermal/flow field. This assumption is reasonably accurate because the particle loading in the HVOF thermal spray process is typically less than 4% (Yang and Eidelman, 1996). In addition, a commonly used assumption that the chemical reaction rate is much faster than the time-scale associated with the gas dynamics (Cheng et al., 2003) is employed in order to make the reactive flow process easier to handle. Based on this assumption, the eddy dissipation model (will be shown later) with a stoichiometry derived from an instantaneous equilibrium code (Li et al., 2004b) is employed to model the combustion process. Regarding the role of the air stream, it is assumed that all the oxygen coming from the air participates in

the reaction (see also Power et al., 1991; Gourlaouen et al., 2000; Dolatabadi et al., 2003; Li et al., 2004b). Gourlaouen et al. (2000) pointed out that the airflow mixing with the oxygen/propylene mixture is more effective in the currently used Diamond Jet hybrid gun than the older Diamond Jet gun, as implied by the "water-cooled" (not "air-cooled") nozzle. It is also assumed that all combustion gases obey the ideal gas law.

The governing equations for the HVOF thermal spray process are the conservation of mass, momentum and energy. The direct solution of these conservation equations for such a high-Reynolds-number turbulent compressible flow is far beyond the current computation capacity. However, by applying Reynold or Favre averaging, these equations can be simplified in such a way that the small-scale turbulent fluctuations do not have to be directly simulated, and consequently, the computational load can be significantly reduced. In Reynolds or Favre averaging, the solution variables are decomposed into the mean (time- or density-averaged) and fluctuating components:

Reynolds (or time) averaging

$$\phi = \bar{\phi} + \phi', \ \ \text{with} \ \bar{\phi} = \frac{1}{\Delta t}\int_{t_0}^{t_0+\Delta t} \phi \, dt \ \text{and} \ \bar{\phi}' = 0. \quad (1)$$

Favre (or density) averaging

$$\phi = \tilde{\phi} + \phi'', \ \ \text{with} \ \tilde{\phi} = \frac{\overline{\rho\phi}}{\bar{\rho}} \ \text{and} \ \tilde{\phi}'' = 0. \quad (2)$$

Substituting the above expressions into the instantaneous continuity and momentum equations, and taking a time average of pressure and density, and density average of all the other quantities, we obtain the following equations written in the Cartesian tensor form:

$$\frac{\partial \bar{\rho}}{\partial t} + \frac{\partial}{\partial x_j}(\bar{\rho}\tilde{v}_j) = 0 \quad (3)$$

and

$$\frac{\partial}{\partial t}(\bar{\rho}\tilde{v}_i) + \frac{\partial}{\partial x_j}(\bar{\rho}\tilde{v}_i\tilde{v}_j)$$
$$= -\frac{\partial \bar{p}}{\partial x_i} + \frac{\partial}{\partial x_j}\left[\mu\left(\frac{\partial \tilde{v}_i}{\partial x_j} + \frac{\partial \tilde{v}_j}{\partial x_i} - \frac{2}{3}\delta_{ij}\frac{\partial \tilde{v}_l}{\partial x_l}\right)\right]$$
$$+ \frac{\partial}{\partial x_j}(-\overline{\rho v_i'' v_j''}), \quad i = 1, 2, 3, \quad (4)$$

where ρ is the density, p is the pressure, x is the coordinate, μ is the molecular viscosity, δ_{ij} is the Kronecker delta and i, j and l are the indices. $-\overline{\rho v_i'' v_j''}$ is the Reynolds stress term representing the effect of turbulence, which can be related to the mean velocity gradients according to the Boussinesq hypothesis:

$$-\overline{\rho v_i'' v_j''} = \mu_t\left(\frac{\partial \tilde{v}_i}{\partial x_j} + \frac{\partial \tilde{v}_j}{\partial x_i}\right) - \frac{2}{3}\left(\bar{\rho}k + \mu_t\frac{\partial \tilde{v}_l}{\partial x_l}\right)\delta_{ij}, \quad (5)$$

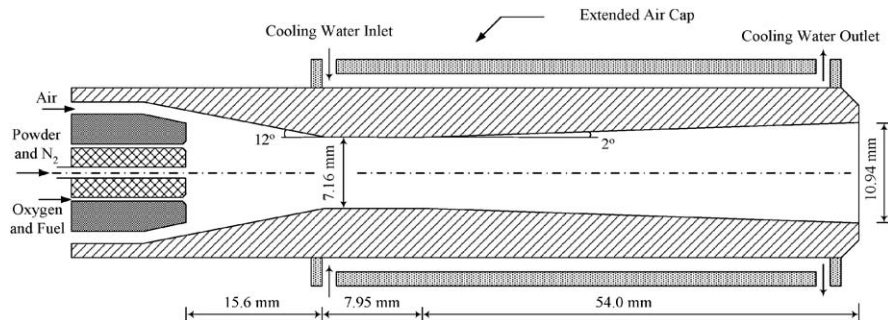where μ_t is the turbulent viscosity and k is the turbulence kinetic energy.

Fig. 1. Schematic diagram of the Diamond Jet hybrid thermal spray gun.

Due to the high Reynolds number and the large pressure gradient in the nozzle, the RNG k–ε turbulence model is used with the non-equilibrium wall function treatment to enhance the prediction of the wall shear and heat transfer. The RNG k–ε turbulence model has the following form:

$$\frac{\partial}{\partial t}(\bar{\rho}k) + \frac{\partial}{\partial x_j}(\bar{\rho}\tilde{v}_j k) = \frac{\partial}{\partial x_j}\left[\alpha_k(\mu+\mu_t)\frac{\partial k}{\partial x_j}\right]$$
$$+ G_k - \bar{\rho}\varepsilon - Y_M \quad (6)$$

and

$$\frac{\partial}{\partial t}(\bar{\rho}\varepsilon) + \frac{\partial}{\partial x_j}(\bar{\rho}\tilde{v}_j\varepsilon) = \frac{\partial}{\partial x_j}\left[\alpha_\varepsilon(\mu+\mu_t)\frac{\partial\varepsilon}{\partial x_j}\right]$$
$$+ C_{1\varepsilon}\frac{\varepsilon}{k}G_k - C_{2\varepsilon}\bar{\rho}\frac{\varepsilon^2}{k} - R_\varepsilon, \quad (7)$$

where ε is the turbulence dissipation rate, G_k is the generation of turbulence kinetic energy due to the mean velocity gradients, Y_M is the contribution of the fluctuating dilatation in compressible turbulence to the overall dissipation rate, R_ε is the additional term in the ε equation. $C_{1\varepsilon} = 1.42$, $C_{2\varepsilon} = 1.68$, and α_k and α_ε are the inverse effective Prandtl numbers for k and ε.

Under chemical reaction, the mass fraction of each species, Y_i, is governed by the following convection–diffusion equation:

$$\frac{\partial}{\partial t}(\bar{\rho}Y_i) + \frac{\partial}{\partial x_j}(\bar{\rho}Y_i\tilde{v}_j) = -\frac{\partial}{\partial x_j}(J_i) + R_i,$$
$$i = 1, \dots, N-1, \quad (8)$$

where J_i is the diffusion flux of species i calculated by Maxwell–Stefan equations, R_i is net rate of production of species i by chemical reaction, and N is the total number of species involved in the reaction.

The energy conservation is described by

$$\frac{\partial}{\partial t}(\bar{\rho}H) + \frac{\partial}{\partial x_i}[\tilde{v}_i(\bar{\rho}H + \bar{p})]$$
$$= \frac{\partial}{\partial x_j}\left[\alpha c_p(\mu+\mu_t)\frac{\partial T}{\partial x_j} + \tilde{v}_i(\mu+\mu_t)\right.$$
$$\left.\left(\frac{\partial\tilde{v}_j}{\partial x_i} + \frac{\partial\tilde{v}_i}{\partial x_j} - \frac{2}{3}\delta_{ij}\frac{\partial\tilde{v}_l}{\partial x_l}\right) - \sum_{i=1}^{N} J_i H_i\right] + S_E, \quad (9)$$

where T is the temperature, H is the total enthalpy defined by $H = \sum_i H_i Y_i$, and S_E is the source term (e.g., heat generated by the exothermic reaction).

2.3. Eddy dissipation model

The combustion of hydrogen is a very complex process. As the temperature increases above 2000 K, CO_2 and H_2O will dissociate into a number of species with low molecular weight due to strong thermal atomic vibration (Cheng et al., 2001b). Previous studies have shown that a combustion model which does not account for the dissociation of combustion products will overpredict the combustion temperature (Oberkampf and Talpallikar, 1996; Gu et al., 2001; Li et al., 2004b). To accurately model the combustion process with tolerable computational efforts, several assumptions were usually made in order to address the chemistry issues, which can be classified into the following three categories: (1) reduced kinetics (Power et al., 1991; Dolatabadi et al., 2003), (2) infinite reaction rate with equilibrium chemistry (Oberkampf and Talpallikar, 1996; Yang and Eidelman, 1996; Hassan et al., 1998; Cheng et al., 2001a,b), and (3) finite reaction rate with equilibrium chemistry (Chang and Moore, 1995; Lopez et al., 1998; Gu et al., 2001). Generally speaking, the finite rate chemistry model is better than the infinite rate one since the latter may result in solution instabilities (Lopez et al., 1998). The eddy dissipation model, which assumes that reactions occur infinitely fast and the reaction rate is limited by the turbulent mixing rate of fuel and oxidant, is employed in this paper. In many practical situations like the HVOF thermal spray process, the eddy-dissipation model describes the limiting rate and thus a knowledge of accurate Arrhenius rate data is not needed. This conclusion has been validated by experimental observations (Dolatabadi et al., 2003). Based on the fact that the gas residence time in the combustion chamber (convergent section of the nozzle) is much longer than the subsequent parts, it is assumed that most of the reaction occurs in the chamber and the reaction moves forward following an equilibrium chemistry model. Assuming that the air is composed of oxygen and nitrogen only, the reaction considered in this paper is of the following

form:

$$\varphi C_3H_6 + 4.5O_2 \Rightarrow \xi_1CO + \xi_2CO_2 + \xi_3H + \xi_4H_2$$
$$+ \xi_5H_2O + \xi_6O + \xi_7OH$$
$$+ \xi_8O_2. \tag{10}$$
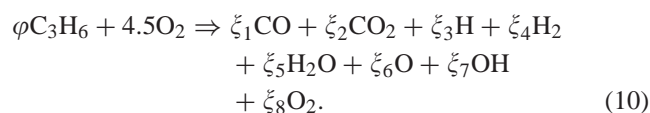
As we pointed out before, the stoichiometric coefficients of each component in the above reaction formula are determined using an instantaneous equilibrium model. However, it is worth noting that the fraction of each species in the combustion gas mixture relies on the combustion pressure, which, in turn, is dependent on the gas flow rate of oxygen, propylene, air and carrier gas at the entrance of the torch. Therefore, several iteration steps are needed to guarantee that the pressure used in deriving the stoichiometry in Eq. (10) is consistent with the pressure eventually determined by CFD modeling. In order to have a good starting point, we use at first a 1-D model (Li et al., 2004b) to calculate the combustion pressure based on the flow rate of each gas stream at the entrance of the HVOF torch, and then solve the stoichiometric coefficient involved in Eq. (10) using a chemical equilibrium code with the combustion pressure equal to the partial pressure of oxygen and propylene (Gordon and McBride, 1994). In this way, the pressure obtained by model in (Li et al., 2004b) is similar to the pressure calculated by CFD simulation, and the work of trial and error can be significantly reduced.

3. Particle dynamics

As we mentioned before, due to the very low particle loading, the coupling between the gas phase and the particulate phase is one-way, i.e., the fluid influences the particles via momentum transfer and heat transfer, but the particles have no influence on the gas phase. Therefore, the particle trajectories, temperature histories and melting degrees can be solved after the gas thermal and flow fields are determined. Particle coagulation in the HVOF thermal spray process has not been reported in literature, which might be explained by the following argument. Based on the analysis of Crowe et al. (1997), the average interparticle spacing ratio in a gas flow field can be estimated by

$$\frac{L_d}{d_p} = \left[\frac{\pi}{6} \frac{1+\kappa}{\kappa} \right]^{1/3}, \tag{11}$$

where L_d is the distance between two particles and κ is the particle/gas mass flow rate ratio divided by the particle/gas density ratio. Usually the particle loading is about 4%, the density ratio is about 10^{3-4}, therefore L_d/d_p is about 20–50, which implies that the individual powder particles can be considered isolated from each other. Therefore, in this work, we assume that particle coagulation is negligible and the powder size distribution does not change during flight.

The motion of particles in the gas flow field is governed by Newton's law, which can be written as

$$m_p \frac{dv_p}{dt} = \sum_i F_i. \tag{12}$$

In typical HVOF thermal spray conditions, the major force acting on a particle is the drag force, and other forces, such as the basset history term, gravitational force, thermophoresis force, and forces caused by pressure gradient and added mass, etc., can be neglected (Power et al., 1991; Pawlowski, 1995). Therefore, the equation of particle motion has the following form:

$$m_p \frac{dv_p}{dt} = \frac{1}{2} C_D \rho_g A_p (v_g - v_p)|v_g - v_p|, \quad v_p = v_{p0}, \tag{13a}$$

$$\frac{dx_p}{dt} = v_p, \quad x_p = x_{p0}, \tag{13b}$$

where m_p is the mass of the particle, v_p is the axial velocity of the particle, t is the time, A_p is the projected area of the particle on the plane perpendicular to the flow direction, ρ_g is the density of the gas, C_D is the drag coefficient, and x_p is the position of the particle. The absolute sign in the relative velocity between particle and gas implies that a particle is accelerated if its velocity is less than that of the gas and decelerated otherwise. In order to take into consideration the fact that many powders used in the HVOF process are not spherical, a formula for the drag coefficient C_D, which accounts for the particle shape using the concept of sphericity ϕ (defined as the ratio of the surface area of a sphere with equivalent volume to the actual surface area of the particle) is used in this paper, which has the following form (Ganser, 1993):

$$\frac{C_D}{K_2} = \frac{24}{Re\,K_1K_2} \left[1 + 0.1118(Re\,K_1K_2)^{0.6567} \right]$$
$$+ \frac{0.4305}{1 + 3305/Re\,K_1K_2}, \tag{14}$$

where K_1 and K_2 are two sphericity-related factors. The local Reynolds number (Re) for this two-phase flow problem is defined based on the relative velocity $Re = d_p \mid v_g - v_p \mid \rho_g/\mu_g$, where d_p is either the particle diameter if the particle is spherical or an appropriate equivalent diameter if the particle is not spherical, and μ_g is the gas viscosity. The above formula for the drag coefficient is recommended by Cheng et al. (2001a).

In the HVOF thermal spray process, the Biot number of the particles (ratio of heat transfer coefficient on the boundary to the internal heat conductance) is typically less than 0.1 for good heat conducting materials (see analysis in Section 5.2), which means that the particles are heated with negligible internal resistance and that the temperature gradients inside them can be ignored. Consequently, the equation

describing the heat transfer between a single particle and the gas reduces to a first-order ordinary differential equation. Depending on the value of particle temperature, different equations are used. With the assumption of negligible particle vaporization, the particle heating can be described as follows:

$$
m_p c_{p_p} \frac{dT_p}{dt}
= \begin{cases} hA'_p(T_g - T_p) + S_h, & (T_p \neq T_m), \\ 0, & (T_p = T_m), \end{cases} \quad T_p = T_{p_0},
$$

(15a)

$$
\Delta H_m m_p \frac{df_p}{dt}
= \begin{cases} hA'_p(T_g - T_p) + S_h, & (T_p = T_m), \\ 0, & (T_p \neq T_m) \end{cases} \quad f_p = f_{p_0},
$$

(15b)

where T_p is the temperature of the particle, A'_p is the surface area of the particle, T_m is the melting point of the particle, ΔH_m is the enthalpy of melting and f_p is the ratio of the melted mass to the total mass of the particle ($0 \leqslant f_p \leqslant 1$). S_h is the source term including heat transfer due to radiation ($\varepsilon \sigma A'_p (T_g^4 - T_p^4)$) and oxidation. The heat transfer coefficient h is computed by the Ranz–Marshall empirical equation:

$$
h = \frac{\lambda_g}{d_p}[2 + 0.6Re^{1/2}Pr^{1/3}],
$$

(16)

where the Prandtl number (Pr) is calculated by $Pr = c_{p_g}\mu_g/\lambda_g$. The thermodynamical and transport properties of the mixture are calculated using the formulas provided in Gordon and McBride (1994). Since the gas properties, such as temperature, velocity, and viscosity are all functions of x_p, if we let $\vec{y} = [v_p, x_p, T_p, f_p]$, Eqs. (13) and (15) can be converted to $d\vec{y}/dt = g(\vec{y})$, $\vec{y}(0) = \vec{y}_0$. This initial value problem can be easily solved by the fourth-order Runge–Kutta method provided that the gas fluid/thermal field is known.

Remark 1. In Rosner (2000), it was pointed out that when the velocity difference ($|v_g - v_p|$) is large, the effective driving force for heat transfer should be ($T_{g_{eff}} - T_g$), where $T_{g_{eff}}$ is the sum of T_g and a fraction of the $(v_g - v_p)|v_g - v_p|/2c_{p_g}$ term, due to the dissipation of gas kinetic energy in the vicinity of each particle. In such a case, not only the heat transfer coefficient is large (due to the Reynolds number term), but also the effective driving force. This effect is not taken into account in the present work, similar to the treatment in previous CFD investigations (for example, Power et al., 1991; Cheng et al., 2001a; Yang and Eidelman, 1996; Dolatabadi et al., 2003). Inclusion of this "viscous dissipation" effect would enhance the heat transfer between the gas phase and the particle phase. However, the qualitative relationship between particle temperature histories and operating conditions will not be affected by this factor.

Remark 2. Note that in the HVOF thermal spray processing of particles consisting of carbides with binding metals, such as the WC–Co powders used in this work, only the latter may experience a molten state because the gas temperature in a conventional HVOF thermal spray process is not high enough for melting carbides, which have high melting points (i.e., 3143 K for tungsten carbide) (Sobolev et al., 1994). In such a case, the particle melting equation in Eq. (15) is modified in such a way that only the fusion of metals might occur in the gas thermal field. In the present work, the melting degree of particles represents the one of the binder (cobalt) instead of the whole particulate phase.

Remark 3. Note that in Eq. (15), we used a first-order ODE to describe particle heating, which holds only when the Biot number (the ratio of thermal internal resistance to surface film resistance) is less than 0.1. This can be verified by the following analysis:

$$
Bi = \frac{hd_p}{6\lambda_p} = \frac{Nu\lambda_g}{6\lambda_p}.
$$

(17)

For tungsten carbide, $\lambda_p = 10^{1-2} \, \text{W/(m K)}$, since $Nu = 10^{0-1}$, $\lambda_g = 0.01$ to $0.1 \, \text{W/(m K)}$, the Biot number is much less than 0.1.

4. Formation of coating microstructure

A thermally sprayed coating consists of lamellar splats interspersed with pores. The splats are the fundamental building blocks of the coating formed by the impact, deformation, spreading and solidification of individual droplets. The pores result from the interaction of the droplets with the previously deposited coating surface. Comprehensive computational modeling of high speed droplet impact on a surface usually involves solution of the time-dependent Navier–Stokes equations (Haller et al., 2002, 2003). In order to increase computation efficiency in this work, the coating growth is modeled by taking advantage of the analysis of Madejski (1976), which shows that as a fully melted particle hits the substrate, the splat becomes a thin cylinder as a result of deformation, and the flattening ratio ξ (defined as $\xi = D/d_p = (2/d_p)\sqrt{\frac{A}{\pi}}$), can be estimated by

$$
\xi = 1.2941Re^{0.2},
$$

(18)

where D and A are the estimated diameter and area of the splat, respectively, d_p is the particle diameter prior to impact, and Re is the Reynolds number ($Re = d_p v_p/v_p$, where v_p is the kinematic viscosity of the droplets). If a particle is partially melted at the point of impact on the substrate, it is assumed in the present work that the unmelted part will form a hemisphere with the equivalent volume and the melted part will form a ring around this hemisphere, whose flattening ratio can also be calculated using Eq. (18).

Based on this approximation, the coating formation is studied using a 2-D model (Shi et al., 2004) in which the cross section of the coating that is perpendicular to the substrate is simulated. The size of each particle is chosen by using a random number generator according to a lognormally distributed particle size distribution, and the velocity, temperature and melting ratio of the single particles at the point of impact on the substrate are calculated using the particle dynamics model developed in the previous section. The lognormal size distribution function is of the following form:

$$f(d_p) = \frac{1}{\sqrt{2\pi}\sigma_{LN}d_p} \exp\left[-\frac{(\ln d_p - \mu_{LN})^2}{2\sigma_{LN}^2}\right], \qquad (19)$$

where $f(d_p)$ is the size distribution function, μ_{LN} and σ_{LN}^2 are two dimensionless parameters corresponding to the mean and the variance of $\ln d_p$, which obeys the normal distribution. For particles that are lognormally distributed, μ and σ can be determined by the following formulas (Li and Christofides, 2003):

$$\mu_{LN} = \ln \sqrt[3]{d_{10}d_{50}d_{90}} - 1.831\left(\ln \sqrt{\frac{d_{90}}{d_{10}}}\right)^2,$$

$$\sigma_{LN} = 0.781 \ln \sqrt{\frac{d_{90}}{d_{10}}}, \qquad (20)$$

where d_{10}, d_{50} and d_{90} are three characteristic diameters which can be obtained experimentally (Lau et al., 1998).

It is assumed that each individual particle is added to the previously formed coating surface until the coating thickness reaches its specified value. The hitting point of each particle follows a uniformly distributed function because the HVOF gun is moving back and forth during operation. Depending on the physical state of the sprayed particle and the condition of the previously deposited coating surface at the point of impact, several different events may occur on the substrate. These events are governed by certain rules shown below:

1. When a particle hits the substrate, the melted part will fit to the surface as much as possible. The splat will move forward until it is in close contact with the previously deposited coating surface.
2. If the unmelted part of a partially melted particle hits at the point of the previously deposited layer that is formed by an unmelted particle, it will bounce off, and a hole will be formed in the center of the disk. Otherwise, it will attach on the coating surface as a hemisphere.
3. If the splat comes to a vertical drop during spreading, the ratio of the splat that has not been settled down will be calculated. If the step does not continue with a gap that can be covered by the splat, the splat will break or cover the corner at the step according to the ratio and the height of the step. Otherwise, the gap will be covered by the splat and a pore will be formed.

4. If the splat encounters a dead end, it will first fill the available space, and then flow over the outer surface depending on the remaining volume.

A detailed discussion of the rule-based modeling of coating growth and coating microstructure was given in our previous work (Shi et al., 2004).

5. Results and discussion

5.1. Analysis of gas dynamics

The process model of gas dynamics was implemented into Fluent, a commercial CFD software, and was solved by finite volume method. The computational domain is shown in Fig. 2. Due to the symmetric geometry of the torch, a one-half, 2-D grid is used. In prescribing the boundary conditions, the flow is radially symmetric at the centerline. In addition, the mass flow rate of oxygen, propylene, air and nitrogen are specified at the openings of each delivery tube. The walls of the torch are all assumed to maintain at a constant temperature of 400 K. In the external flow field, the radial extent of the computational domain is chosen to be 50 mm (more than nine times the radius of the torch exit), which is sufficiently far from the jet outer radius and thus pressure far-field conditions can be applied at the outer boundaries. At the outer boundary which is 0.3 m far away from the torch exit, a pressure outlet boundary condition is specified. Finally, the atmospheric pressure is assumed to be 1.01×10^5 Pa. The computational grid consists of 30 radial and 80 axial nodes inside the torch and 45 radial and 200 axial nodes outside the torch. The grid is highly clustered near the exit of the torch in order to capture the shock diamonds in the external flow field and lowly clustered in the far field. The gas pressure, velocity and temperature in the computational domain is initially patched using linear field functions to accelerate convergence. The governing mass, momentum and energy balance equations together with the ideal gas state equation are solved at first using a first-order upwind scheme to get to a convergent solution and then a second-order upwind scheme to capture the shock diamonds that occur in the external flow field. The baseline gas flow rates of oxygen, propylene, air and carrier gas used in the CFD simulation are shown in the first row of Table 1, which is the recommended flow rate for the processing of Tungsten Carbides. It can be found out that the equivalence ratio (fuel/oxygen ratio divided by its stoichiometric value) is 1.045 and propylene is in excess. We first use a 1-D process model (Li et al., 2004b) to calculate the chamber pressure and then use a chemical equilibrium program code developed by Gordon and McBride (1994) to get the reaction formula under a partial pressure of oxygen and propylene. Subsequently, we run the CFD simulation and compare the final pressure with the one used for deriving the reaction
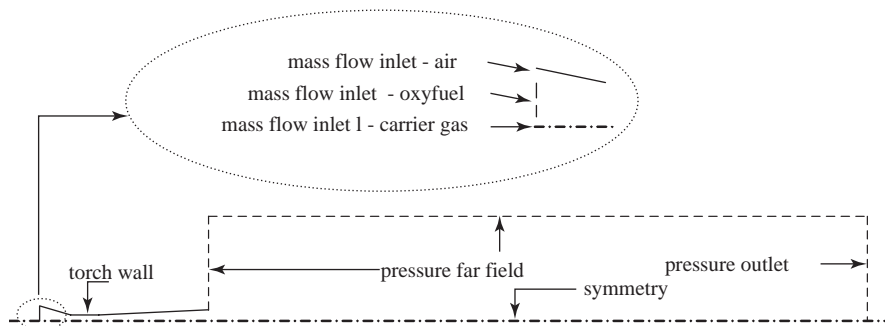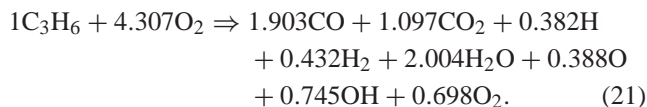
Fig. 2. Computational domain and boundary conditions.

Table 1
Specified gas flow rate for parametric analysis of Diamond Jet hybrid HVOF gun

Case	Propylene (scfh)	Oxygen (scfh)	Air (scfh)	Nitrogen (scfh)	$\dot{m}$ (g/s)	φ
1 (Baseline)	176	578	857	28.5	18.10	1.045
2	176	578	428	28.5	13.73	1.186
3	176	867	857	28.5	21.35	0.756
4	264	867	1286	28.5	27.01	1.045

formula. Trial and error shows that the chamber pressure is about 6.0×10^5 Pa and the partial pressure of oxygen and propylene is about 3.4×10^5 Pa, under which the equilibrium stoichiometry is

$$1C_3H_6 + 4.307O_2 \Rightarrow 1.903CO + 1.097CO_2 + 0.382H$$
$$+ 0.432H_2 + 2.004H_2O + 0.388O$$
$$+ 0.745OH + 0.698O_2. \qquad (21)$$

Note that propylene does not appear at the right-hand side of the reaction formula under normal operating conditions. Furthermore, O_2 appears in the right-hand side of the reaction because it is not completely consumed under equilibrium conditions.

The simulated contours and centerline profiles of static pressure, mach number, axial velocity and temperature in the internal and external fields are shown in Fig. 3. In the combustion chamber (convergent section of the air cap), reaction of the pre-mixed oxygen and propylene results in an increase of gas temperature above 3000 K and a pressure of 6.0×10^5 Pa is maintained. As the exhaust gases expand through the convergent–divergent nozzle, the pressure decreases and the gas velocity increases continuously. At the throat of the nozzle, the Mach number is close to 1. The gas is accelerated to supersonic velocity in the divergent section of the nozzle and reaches a Mach number of 2 at the exit of the nozzle.

As we stated before, depending on the magnitude of the total temperature and total pressure at the chamber as well as the temperature and velocity at the nozzle exit, the flow condition at the exit of the nozzle may be underexpanded, ideally expanded or overexpanded. Our simulation shows that the pressure at the exit of the air cap is 6×10^4 Pa, which

implies that the flow is overexpanded. The manufacturer, Sulzer Metco measured a gauge pressure of -3×10^4 Pa, (or the absolute pressure is about 7×10^4 Pa) at the nozzle exit under the same operating conditions (Mills, 2003), which partially validates the modeling assumptions used in the present work. In fact, the overexpanded flow condition gives a slightly higher gas velocity, and more kinetic energy can be transferred to the powders. The overexpanded flow pattern involved in the HVOF thermal spray process can be illustrated by Fig. 4. At the exit of the nozzle, the shock front begins obliquely as a conical surface and is cut off by a "Mach shock disc" perpendicular to the axis. Behind the incident and Mach shock front, a reflected shock front and a jet boundary develop. As the reflected shock front meets the jet boundary, reflected expansion waves develop. These reflected expansion waves converge before reaching the opposite boundaries and give rise to shock fronts, which meet the jet boundary again and the whole process repeats. This periodic jet pattern is eventually blurred and dies out due to the action of viscosity at the jet boundary.

We note that although the gas temperature inside of the torch is very high, its value in the centerline, however, is less than that outside of the torch. This also implies that the external thermal field plays a very important role in particle heating. The contour of gas temperature in the external field is given in Fig. 5. It is shown that the gas temperature is relatively low at the exit of the torch (approximately 1800 K). However, passing through the first shock leads to a sharp increase in the gas temperature (approximately 2600 K). The location of the first shock is 7 mm, which is a little higher than the reported measured value (5 mm) in which a similar
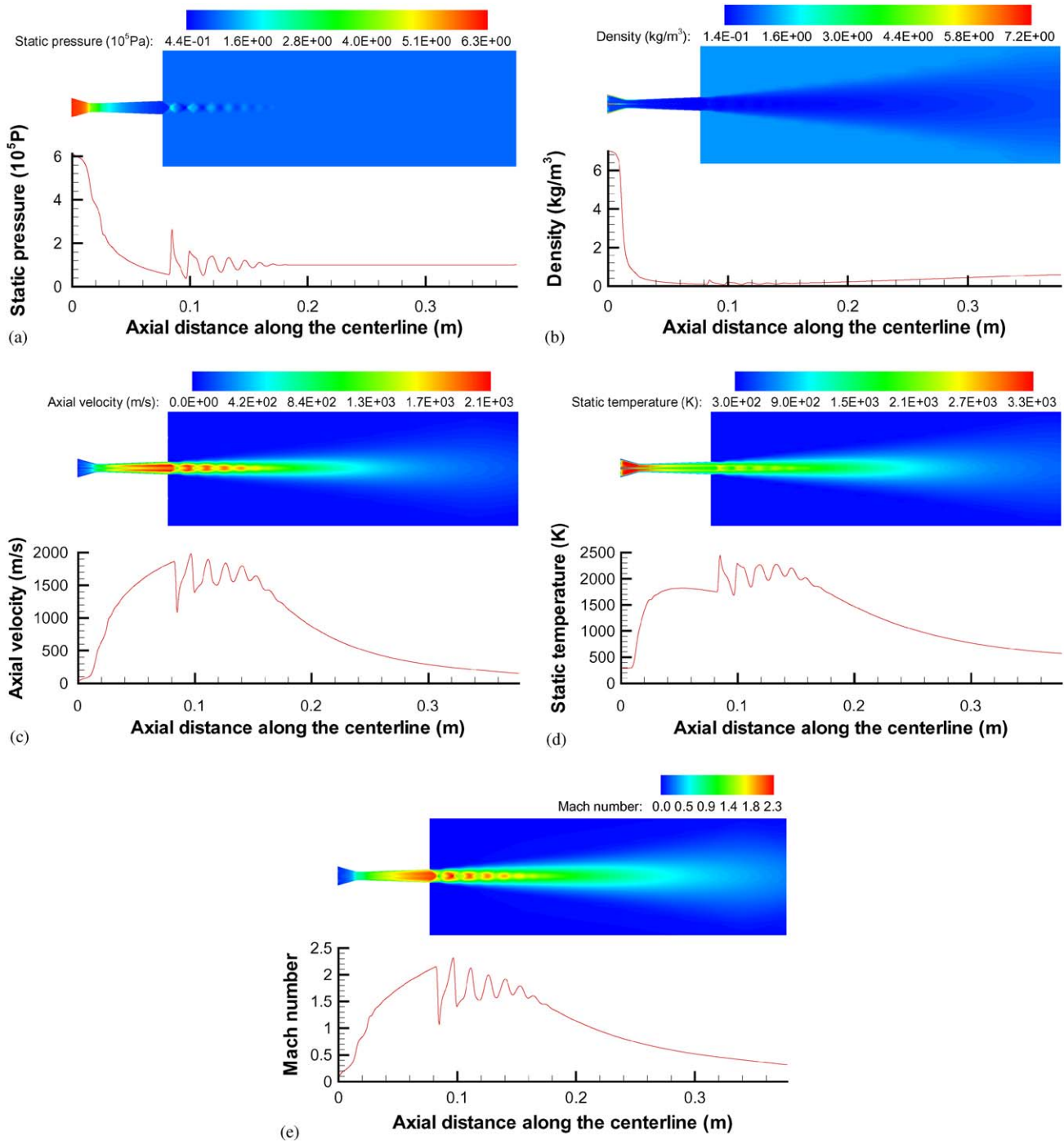
Fig. 3. Contours of flooded gas properties (upper plot) and centerline profiles of gas properties (lower plot): (a) static pressure, (b) density, (c) axial velocity, (d) static temperature, and (e) mach number.

operating condition but with a lower flow rate of propylene and nitrogen is used (Dolatabadi et al., 2003).

A previous study of Power et al. (1991) has demonstrated the cooling effect of air in the former Diamond Jet gun (without extended air cap). This unique behavior can also be observed in the current Diamond Jet hybrid gun (with the extended air cap). It can be easily seen in Fig. 6 that the

hot flame is surrounded by the cooling air around the torch wall, thus protecting the hardware from being overheated.

The solved mole fraction of each gas component is shown in Fig. 7. In the first 1 cm, only nitrogen exists in the centerline, which comes from the carrier gas. Due to turbulent mixing, the mole fraction of nitrogen decreases gradually and the mole fractions of all the other species increase as the
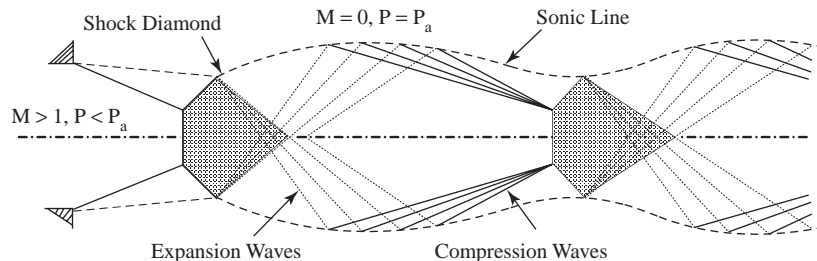
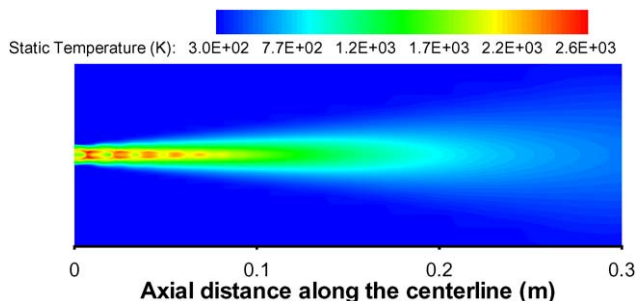Fig. 4. Schematic of wave structure in the overexpanded jet.

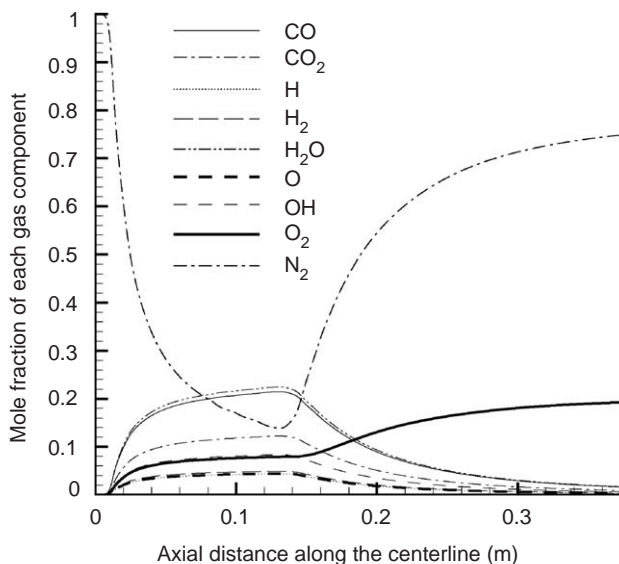Fig. 5. Contour of static temperature outside of the torch.

Fig. 6. Contour of static temperature in the combustion chamber.

Fig. 7. Mole fraction of each gas component along the centerline.

Based on the proposed CFD model, a parametric analysis is performed in order to study the effect of gas flow rate on the gas dynamics, and the simulation results under different gas flow rates (see Table 1) are shown in Fig. 8. The reaction formulas determined by the iterative procedure proposed in Section 2.3 and used in the eddy-dissipation model for these four cases are shown in Table 2. Generally speaking, as the mass flow rate increases, the pressure will increase, which might be explained by the following equation:

$$\dot{m}_g = \rho_t v_t A_t = \frac{P_0}{\sqrt{T_0}} A_t \left[\frac{\gamma \bar{M}_{pr}}{R} \left(\frac{2}{\gamma+1} \right)^{(\gamma+1)/(\gamma-1)} \right]^{1/2},$$
(22)

where $\dot{m}_g$ is the total mass flow rate, $\bar{M}_{pr}$ is the average molecular weight of the gas mixture after reaction, and T_0 and P_0 are the stagnation temperature and the stagnation pressure, respectively. Since $\sqrt{T_0}$ varies much less than m_g, the pressure is approximately proportional to the total mass flow rate. As the pressure increases, the equilibrium temperature of the reaction will go up if the equivalence ratio (fuel/oxygen ratio divided by its stoichiometric value) remains the same. However, it is important to note that the

gas mixture passes through the convergent–divergent nozzle. In the supersonic free jet, because of the entrainment of the air from the external environment, the mole fraction of both nitrogen and oxygen increases and eventually reaches a value of 0.75 and 0.20, at the 0.3 m standoff. It is also shown that the mole fraction of propylene is no more than 10^{-6} along the centerline, which implies that the propylene is almost exhausted by the combustion process, although the process is under fuel-rich condition. Instead, it is shown that the mole fraction of oxygen molecule and oxygen atom in the entire flow field is about 0.1–0.2, which implies that the oxygen may have a significant influence on the particle composition and temperature at impact via particle oxidation.
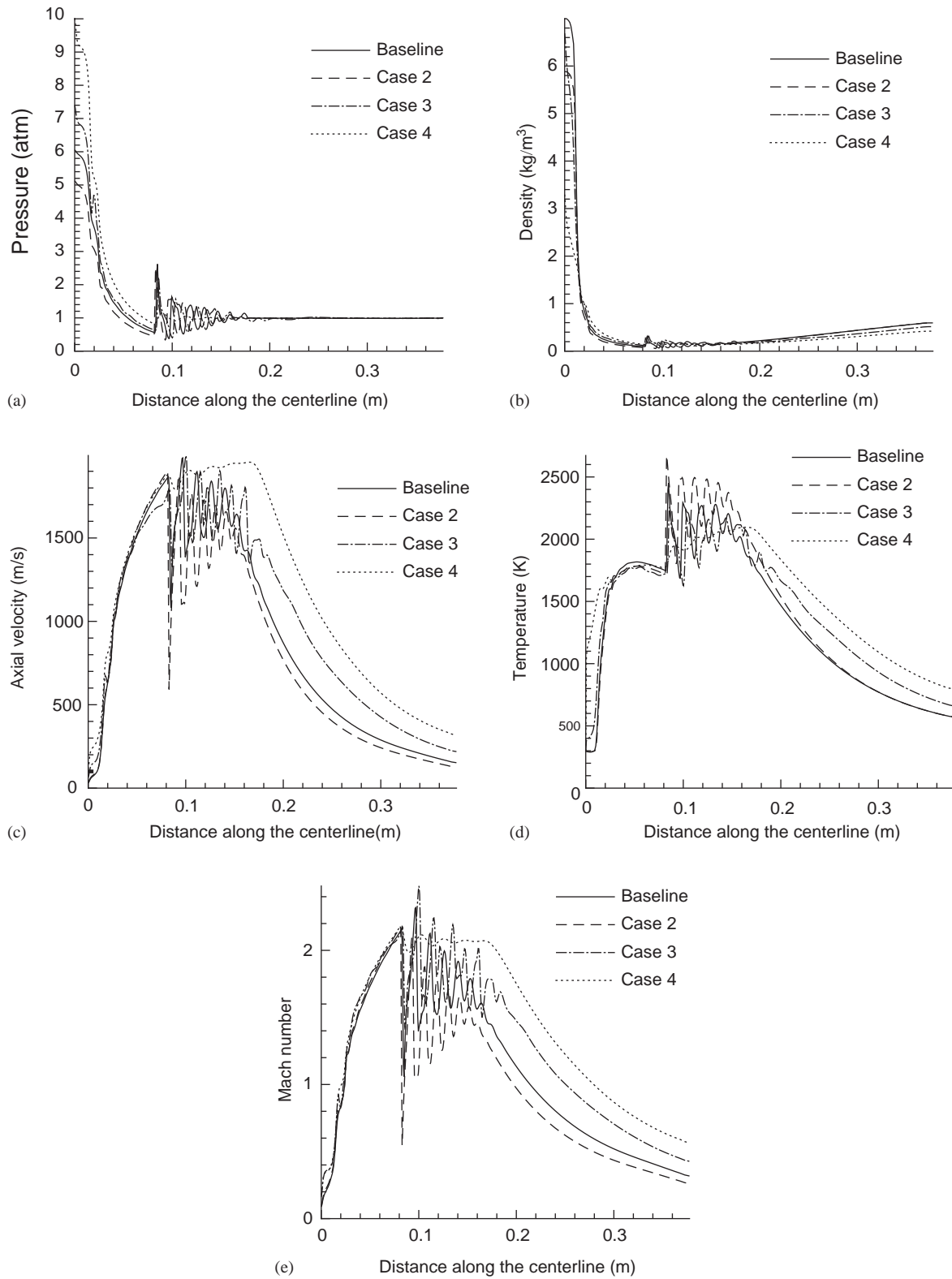
Fig. 8. Influence of gas flow rates on gas properties: (a) static pressure, (b) density, (c) axial velocity, (d) static temperature, and (e) mach number in the centerline.

flame temperature is primarily dependent on the equivalence ratio and high temperatures are achieved at equivalence ratios close to 1.2 (Li et al., 2004b), which may explain the

fact that the gas temperature in case 2 is higher than in the other cases, although the total mass flow rate is the lowest. However, one of the most prominent consequences of

Table 2
Reaction formula obtained from equilibrium chemistry

Case	$P(10^5$ Pa)	Reactants		Products							
		C_3H_6	O_2	CO	CO_2	H	H_2	H_2O	O	OH	O_2
1	3.4	1	4.307	1.903	1.097	0.382	0.432	2.004	0.388	0.745	0.698
2	3.6	1	3.795	2.085	0.915	0.433	0.544	1.918	0.302	0.643	0.413
3	4.7	1	5.949	1.417	1.583	0.248	0.245	2.183	0.538	0.899	1.860
4	5.7	1	4.307	1.860	1.140	0.322	0.406	2.059	0.344	0.747	0.670

increased total gas flow rate is the maintenance of velocity and temperature in the free jet at high levels for a longer distance, which leads to enhanced momentum transfer and heat transfer between the gas phase and the particles. For example, in the last case where the air, oxygen and fuel flow rates are 50% higher than in the baseline conditions, the flow outside of the torch is nearly ideally expanded. As a result, both the centerline velocity and temperature are relatively constant inside the potential core of the jet, whose length is about 8.5 times the diameter of the torch exit. In addition, a relatively low flow rate of the carrier gas will shorten the length of the initial cool zone in the chamber, which will certainly increase the particle temperature, and in turn will affect the coating properties.

Remark 4. In (Li et al., 2004a,b), we developed a simplified 1-D mathematical model for the Diamond Jet hybrid thermal spray process. A comparison of the results obtained by the 1-D model and the CFD model (see Fig. 9) shows that the velocity and temperature predicted by the 1-D model are higher than those predicted by the CFD model, especially in the convergent part of the torch. This can be explained by the large gradient of velocity, temperature and density in the combustion chamber, due to the mixing of cold air and nitrogen with the high-temperature combustion gases. In the chamber, a 1-D model is insufficient to capture the multi-dimensional behavior of the gas phase, especially the temperature and the density (see Figs. 3 and 6 for details). Moreover, because the flow at the exit of the torch is over-expanded but not ideally expanded, the velocity and temperature decay model derived from experiments cannot accurately describe the gas properties in the shock waves, where the centerline velocity and temperature show a sharp fluctuation. Finally, a 1-D model cannot incorporate the influence of the substrate on the gas flow/thermal field, which will be shown in the next subsection. However, the relationship between particle in-flight behavior and gas flow rate, spray distance, etc., can still be reasonably predicted by the simplified 1-D model. Moreover, from a control point of view, a 1-D model is more tractable and its solution time is comparable to the evolution of the process.

### 5.2. Analysis of particle in-flight behavior

The particle temperature plays an important role in the formation of the coating microstructure. Especially in the fabrication of nanostructured coatings, it is crucial to maintain high particle temperatures at the point of impact on the substrate and to prevent particles from being superheated at the same time, because it is exactly the small grain size that leads to the superior qualities of nanostructured coatings (Cheng et al., 2001a). It is also of great importance to maintain high particle velocity at the point of impact on the substrate since the higher the particle velocity, the denser the coating. In order to calculate the particle properties in the gas field, it is important to note that when the substrate is placed downstream of the free jet, the gas flow pattern will be changed because the jet will have a zero axial velocity component at the point of impact on the substrate. To illustrate this, we run two other simulations with the "pressure outlet boundary condition" set to be "wall condition" at the impact and all the other boundary conditions kept the same. The simulation results are shown in Fig. 10. At long spray distances, such as 0.3 m, the substrate has a minimal influence on both the thermal and the flow field. This is because the gas velocity and temperature are relatively low when the spray distance is long. However, as the spray distance becomes shorter, the interaction between the gas and the plate will have a discriminable effect on the gas phase, especially the gas velocity.

The particle in-flight behavior is then solved (particle thermophysical properties are given in Table 3) applying the baseline flow rates given in Table 1 and a spray distance of 0.2 m. The results are shown in Fig. 11, where also the profiles of gas velocity and temperature are given for reference. It is shown that particles of small sizes may reach very high velocities during flight, however, their velocities drop more sharply than those of larger particles because of their smaller momentum inertias. For example, a particle with a diameter of 0.5 μm may reach a velocity of about 1800 m/s during flight, however, its velocity decays very sharply and it is eventually trapped by the gas stream. For a different type of particle with a smaller density (Nickel, for example), the maximum size of particles that will fully track the gas stream may be even larger. Moreover, in the shock waves, where the gas velocity oscillates very sharply, the velocity profiles of small particles show a wave constant trend due to mass inertia, and the particle velocity can exceed the gas velocity at those points. On the other hand, particles of small sizes may be heated to the melting point in a short time and be fully melted during flight, however, they may eventually
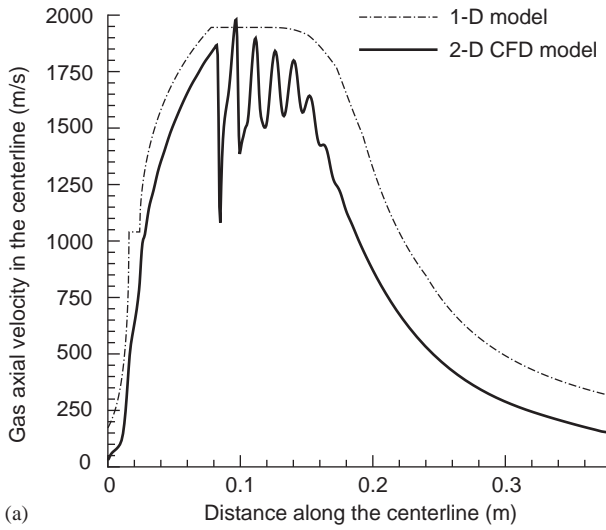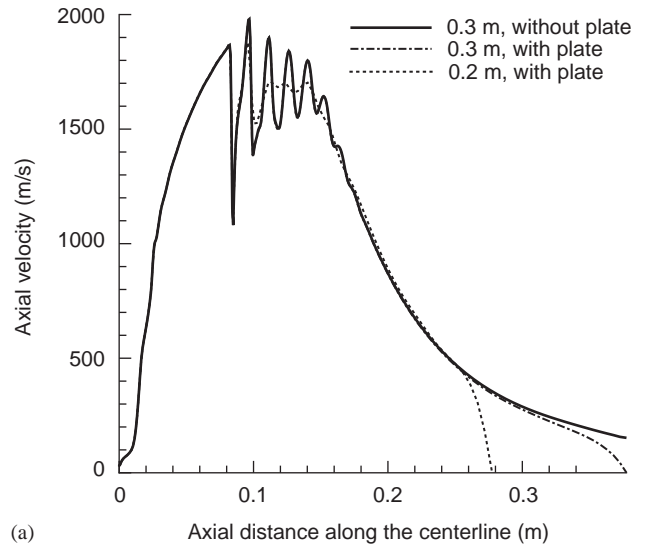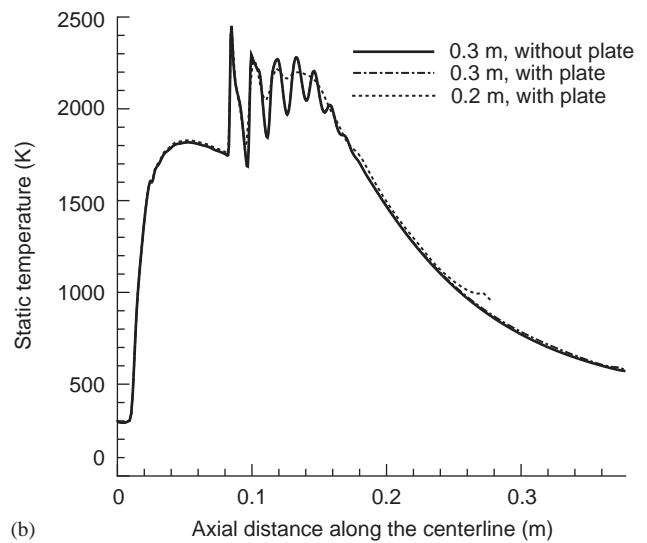
(a)
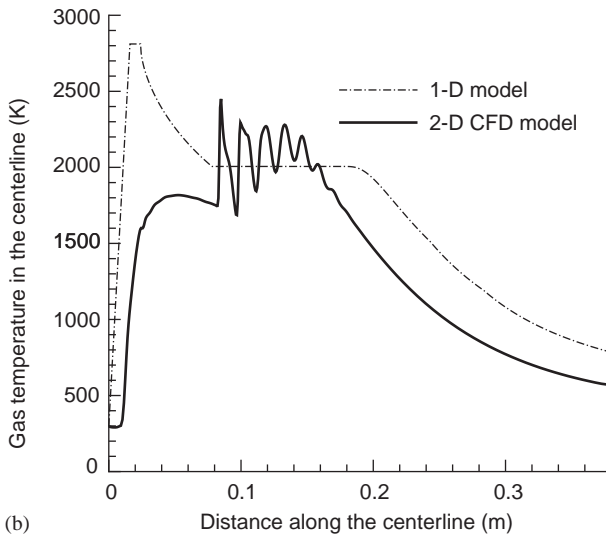
(b)
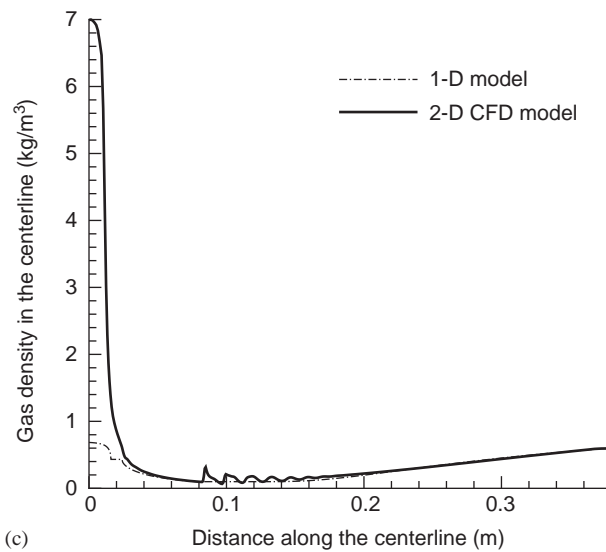
(c)

Fig. 9. Comparison of (a) axial velocity, (b) temperature, and (c) density of gas phase in the centerline using a simplified one dimensional model (Li et al., 2004 a,b) and the CFD model.

(a)

(b)

Fig. 10. Influence of the substrate on the (a) axial velocity, and (b) static temperature in the centerline.

Table 3
Thermophysical properties of WC–12%Co particles (Sobolev et al., 1994)

Density, ρ_p (kg/m^3)	14320
Heat capacity, c_{p_p} (J/kg K)	295.4
Latent heat of fusion, ΔH_m (J/kg)	4.2×10^5
Surface emissivity, ε	0.4
Melting temperature of Cobalt, T_m (K)	1768

be in a coexistence state of liquid and solid or even in a solid state after a long enough distance. Smaller particles tend to change their temperatures easily because of their smaller thermal inertias. The smaller the particle size is, the easier its temperature varies. For particles of large sizes, however, the periods for acceleration and heating are longer and their velocity (or temperature) profiles become nearly flat as
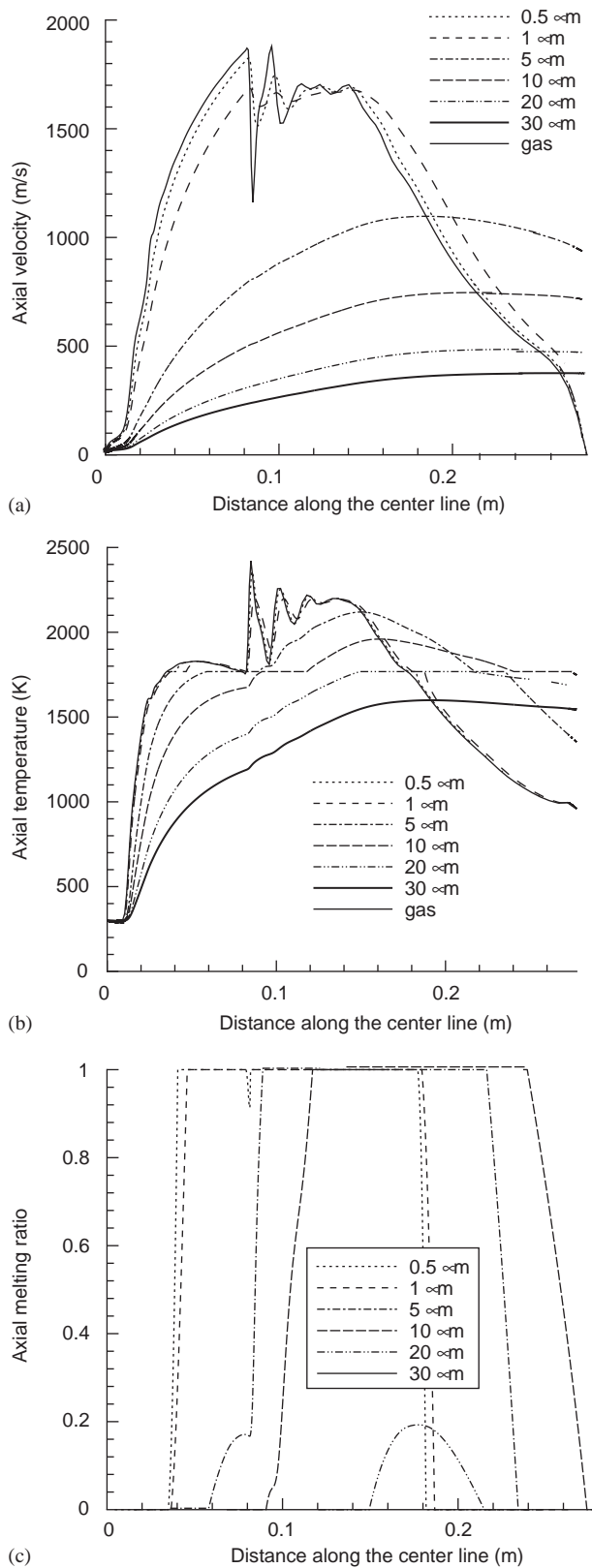
(a)

(b)

(c)

Fig. 11. Profiles of (a) particle velocity, (b) temperature, and (c) melting ratio along the centerline.
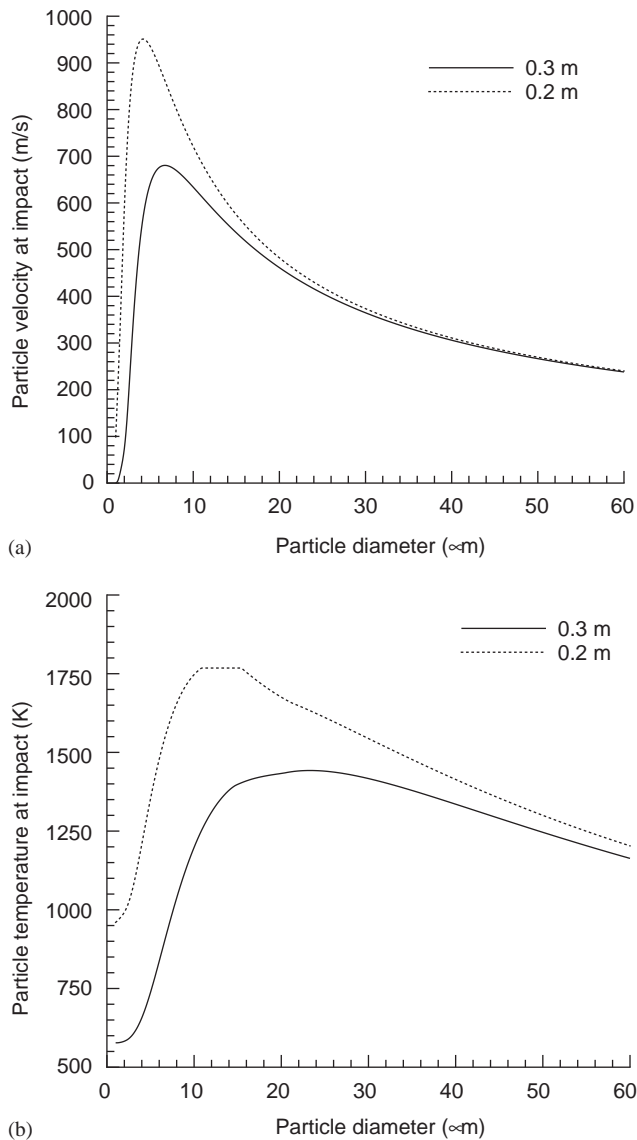

(a)

(b)

Fig. 12. (a) velocity, and (b) temperature of particles of different sizes under 20 m/s injection velocity and different spray distances.

they approach the same velocity (or temperature) of the gas. Moreover, they may not reach the melting point and keep the solid state along the whole flow field. However, particles of medium sizes may become partially melted during flight.

To further understand the behavior of particles in the HVOF process, we also plotted the velocity, temperature and melting ratio at the different spray distances as a function of particle size (see Fig. 12). For all spray distances observed, there is a peak in each of the v_p vs. d_p curves. As the particle diameter increases, the particle velocity increases first, reaching a peak value before decreasing gradually. Generally speaking, changes in the spray distance have a stronger influence on small particles than on big ones. As the spray distance increases, the velocity of small particles at the point of impact on the substrate decreases, which is caused by the

velocity decay of the free jet. However, the velocity of large particles may increase a little as the spray distance increases, although it is hard to discern from Fig. 12. The change in the spray distance may have a broader and stronger influence on the particle temperature. At a short spray distance (10 cm, for example), particles of several micrometers may be fully melted. However, as the spray distance increases, they may be partially melted or even be in a solid state at impact because they solidify as a result of the temperature decay on the free jet. For particles in the range of 10–20 μm, although a change in the spray distance has a negligible influence on their velocity, its strong effect on their temperature can be easily observed. The influence of the spray distance on the particle temperature can be explained by the change of the residence time of particles in the gas flame.

Fig. 13 shows the influence of particle injection velocity on the profiles of particle velocity and temperature. It can be seen that the injection velocity has a negligible influence on the impact velocity for particles in the whole size range of 1–60 μm. It also has a negligible effect on the temperature of small particles at the point of impact on the substrate. The influence of injection velocity on particle temperature becomes visible as the particle diameter goes beyond 30 μm.

The above phenomena can be partially explained by the following mathematical analysis. It is important to note that for large particles ($d_p \geqslant 20$ μm in this case), the particle velocity profile becomes almost flat after an initial acceleration stage, where $v_p \ll v_g$ holds. When the particle velocity approaches the gas velocity, the drag force term becomes small and the particle velocity profile becomes almost flat. Dividing Eq. (13a) by Eq. (13b) and incorporating the definition of the Reynolds number, one can derive

$$\frac{\mathrm{d}v_p^2}{\mathrm{d}x_p} = \frac{3\mu_g C_D Re}{2\rho_p d_p^2}(v_g - v_p).$$

(23)

Approximating $(v_g - v_p)$ by v_g, Eq. (23) can be analytically solved to yield:

$$v_p = \sqrt{\int_0^{x_p} \frac{3\mu_g C_D Re}{2\rho_p d_p^2} v_g \, \mathrm{d}x_p + v_{p_0}^2}$$

$$\approx \sqrt{\int_0^{x_p} \frac{3\mu_g C_D Re}{2\rho_p d_p^2} v_g \, \mathrm{d}x_p}$$

(24)

because the magnitude of the first term is much less than the second one under the square root in Eq. (24) (Li et al., 2004c). Eq. (24) clearly shows that the initial particle velocity has a neglige effect on particle velocity at impact. A similar analysis of particle temperature at impact is easy to carry out and will be omitted here.

Furthermore, if the characteristic time for particle motion $\tau = 4\rho_p d_p^2/3\mu_g C_D Re$ is nearly a constant, an analytic
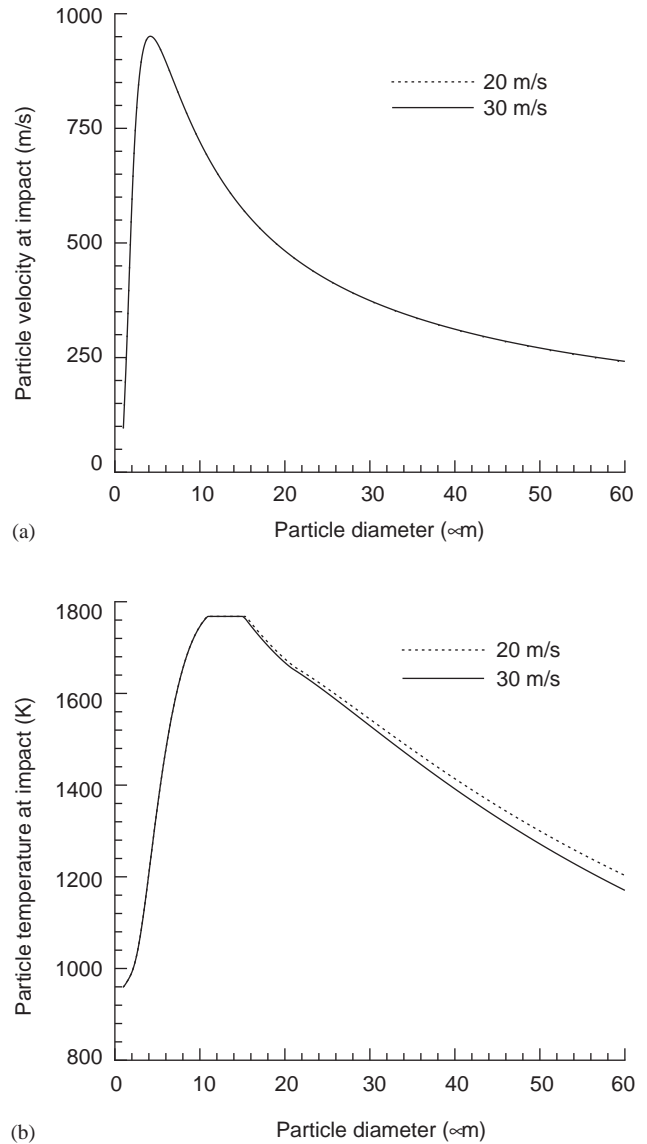

(a)

(b)

Fig. 13. (a) velocity, and (b) temperature of particles of different sizes under 0.2 m spray distance and different injection velocities.

solution of Eq. (13b) can be obtained

$$v_p = e^{-t/\tau}\left[v_{p_0} + \int_0^t e^{t'/\tau}\frac{v_g(t')}{\tau}\,\mathrm{d}t'\right]$$

$$= v_g - (v_{g_0} - v_{p_0})e^{-t/\tau} - e^{-t/\tau}\int_0^t e^{t'/\tau}\frac{\mathrm{d}v_g(t')}{\mathrm{d}t'}\,\mathrm{d}t'$$

$$= v_g - (v_{g_0} - v_{p_0})e^{-t/\tau} - \frac{M}{\tau}(1 - e^{-t/\tau}),$$

(25)

where M is a scalar satisfying $|M| \leqslant |\mathrm{d}v_g/\mathrm{d}t|_{\max}$. It can be concluded from Eq. (25) that the smaller the characteristic time τ, the easier the particle velocity varies. In particular, for very small τ (or particles of small size or density), $v_p \approx v_g$, which implies that the particles will fully track the gas. A similar analysis can be made on particle heating equation by setting $\varpi = d_p^2 \rho_p c_{p_p}/6\lambda_g Nu$, the characteristic time for

particle heating. However, note that because the ratio of these two characteristic time scales

$$\frac{\varpi}{\tau} = \frac{c_{p_p}\mu_g C_D Re}{8\lambda_g Nu} \approx \frac{2.3\mu_g c_{p_p} Re^{0.4}}{\lambda_g Nu} \tag{26}$$

is usually less than one (Li et al., 2004c), it can be concluded that the particle temperature is easier to vary than the particle velocity. Moreover, if ignoring the particle melting behavior, one can derive that

$$\frac{dT_p}{dv_p} = \frac{\tau(T_g - T_p)}{\varpi(v_g - v_p)} \tag{27}$$

which implies that v_p/T_p can be regulated by adjusting gas velocity and temperature. Since the gas velocity is relatively low in the convergent part of the nozzle, the particle heating will be significantly improved if the gas temperature is maintained at high levels by decreasing the carrier gas flow rate (see Fig. 8(d)).

In the industrial HVOF processing environment, it is important to independently control the particle velocity and the particle temperature (or melting degree) in order to achieve desired coating properties. Manipulation of the particle velocity and the particle temperature can be achieved by adjusting the gas momentum flux and the gas temperature. From Eq. (13a) and (15), one can see that the gas momentum flux is approximately proportional to the drag force, and the temperature difference is proportional to the heat transfer rate between gas and particles. Fig. 14 demonstrates the influence of the gas flow rates on the gas momentum flux and the gas temperature based on the simulation results in Section 5.1. It is obvious that the momentum flux increases with the total mass flow rate and that the temperature in the free jet is highly dependent on the equivalence ratio as well as the total flow rate. Therefore, in industrial applications, it is beneficial to increase the total mass flow rate and to keep the equivalence ratio close to 1.2. This conclusion can be substantiated by the simulation results of particle in-flight behavior at a standoff of 0.2 m under various gas flow rates, which are shown in Fig. 15. Generally speaking, the particle velocity increases as the total mass flow rates increase, since high gas momentum flux can be achieved at high gas flow rates, especially in the free jet. The same trend is observed for the particle temperature and degree of melting. However, it is worth noting that the total mass flow rate is not the sole factor affecting particle temperature. For example, the total gas flow rate is the lowest in case 2. However, the particle temperature achieved in this case is even higher than the one in cases 1 and 3, which clearly shows that the equivalence ratio is a key parameter that can be manipulated to adjust particle temperature and degree of melting.

5.3. Analysis of coating microstructure formation

At impact, the particle kinetic energy might be partially converted to thermal energy and the particle temperature
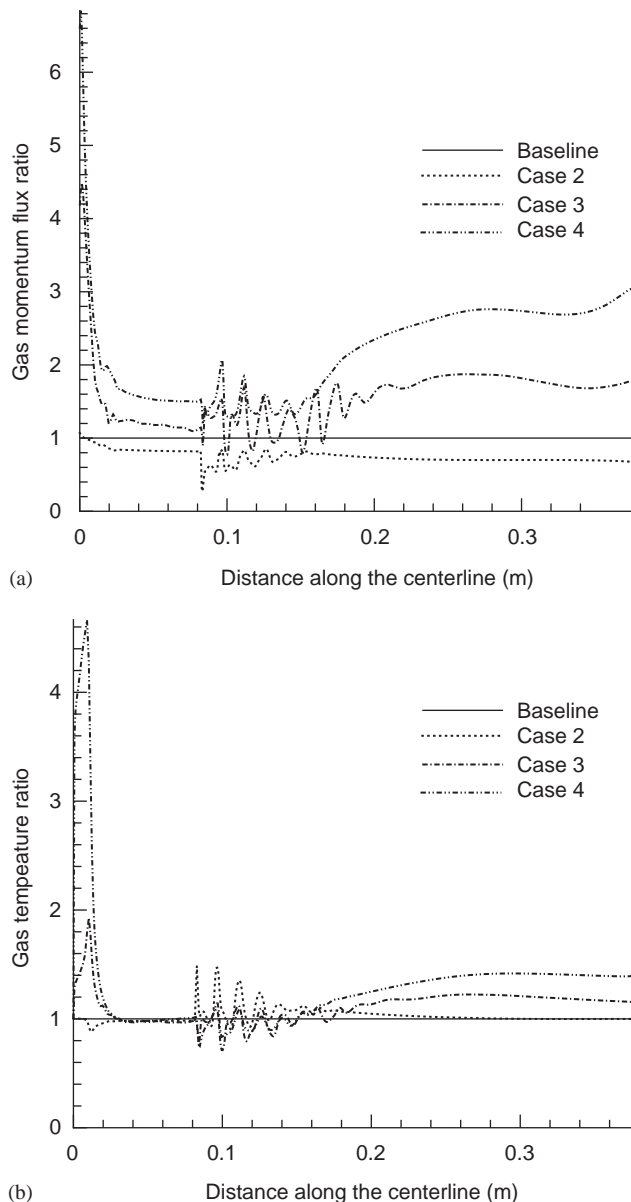

(a)

(b)

Fig. 14. (a) gas momentum flux, and (b) gas temperature along the centerline under different gas flow rates. Normalization is done with respect to the corresponding properties under baseline gas flow rates.

and melting degree will increase due to collision with the coating surface. If 100% conversion efficiency is assumed, the increase in the particle temperature and melting degree can be estimated by the following equation:

$$\frac{1}{2}m_p v_p^2 = \int_{T_1}^{T_2} m_p c_{p_p}\, dT + \int_{f_{p_1}}^{f_{p_2}} \Delta H_m m_p\, df_p, \tag{28}$$

where T_1, f_{p_1} and T_2, f_{p_2} are the temperature and melting ratio before and after impact, respectively.

Based on this approximation, the coating build-up is modeled using stochastic simulation. In the simulation, the coating cross section is assumed to be a rectangle and is discretized using a 8192×4096 mesh. The size of each grid
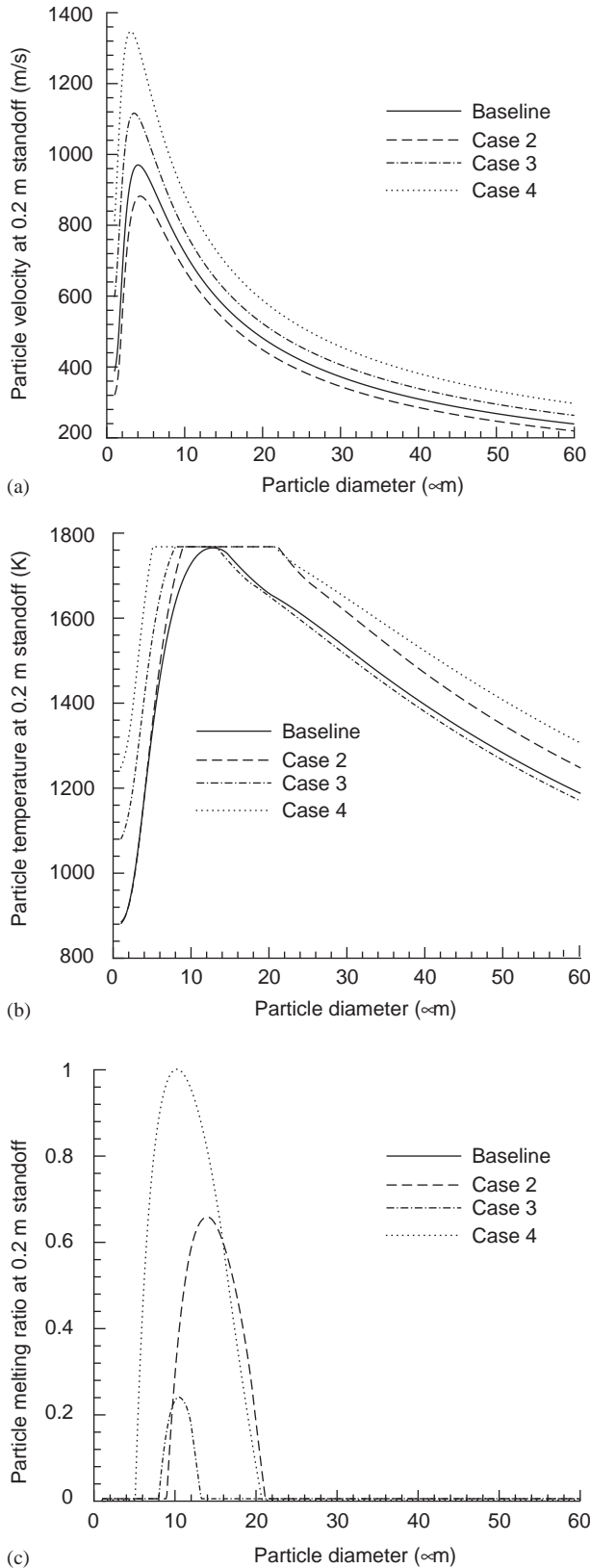
(a)

(b)

Fig. 15. (a) velocity, and (b) temperature of particles of different sizes at 0.2 m standoff under different gas flow rates.
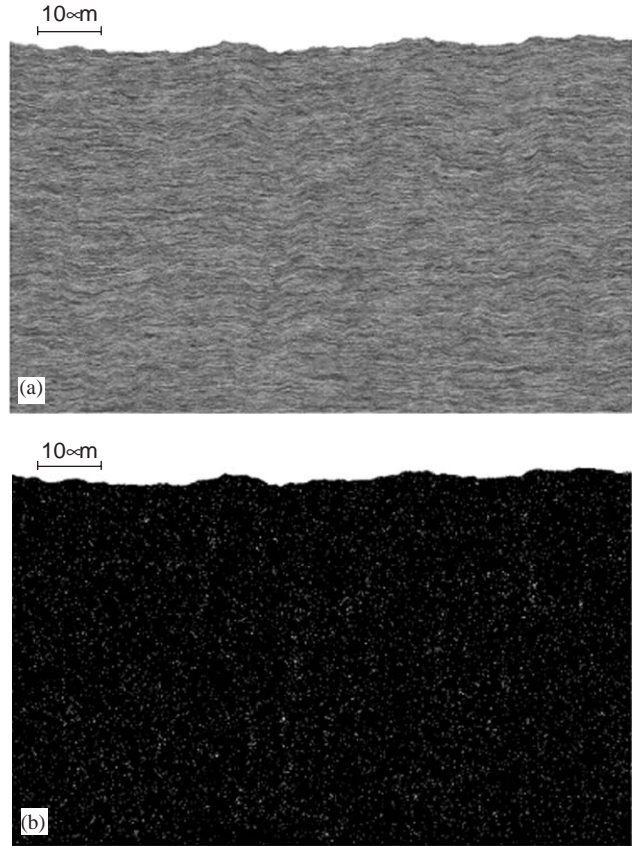

Fig. 16. Simulated (a) microstructure, and (b) pore distribution in the coatings made of fully melted particles (ideal case).

in the mesh is $0.1 \times 0.1 \, \mu m$. The particles are assumed to be lognormally distributed with $d_{10} = 4 \, \mu m$, $d_{50} = 12 \, \mu m$, and $d_{90} = 36 \, \mu m$. If all the particles are fully melted, which is the ideal case, the ideal lamellar coating microstructure is obtained (see Fig. 16). However, both our CFD simulations and analyses as well as the experiments (Zhang et al., 2003) show that particles at the point of impact on the substrate may be in different melting states (fully melted, partially melted or solid) due to different sizes and different trajectories in the HVOF flow field. When this fact is taken into account, the ideal coating microstructure is found to be disturbed by the unmelted fraction of particles. Figs. 17 and 18 show the simulated configuration of the coatings deposited under the first (baseline) and the fourth condition, respectively. It is also shown that unmelted particles affect the coating surface dramatically, thus, leading to a higher porosity and roughness. A comparison of microstructure of coatings fabricated under different flow rates show that when the particle melting ratio is not high, many large particles are bounced off as they hit the substrate. As a result, the deposited coating has a high porosity, for example, 4.6% under the baseline conditions as compared to 1.1% under the conditions in case 4. However, when the particle melting ratio is high, the unmelted particles or the unmelted part of partially melted particles have a high probability
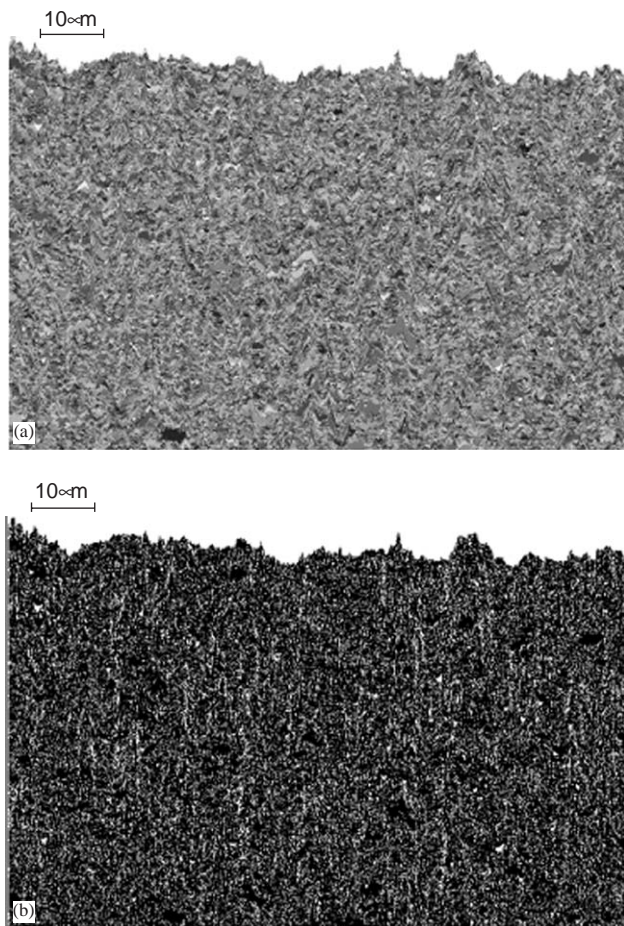
Fig. 17. Simulated (a) microstructure, and (b) pore distribution in the coatings made of particles of nonuniform molten states, which are deposited under the baseline conditions.
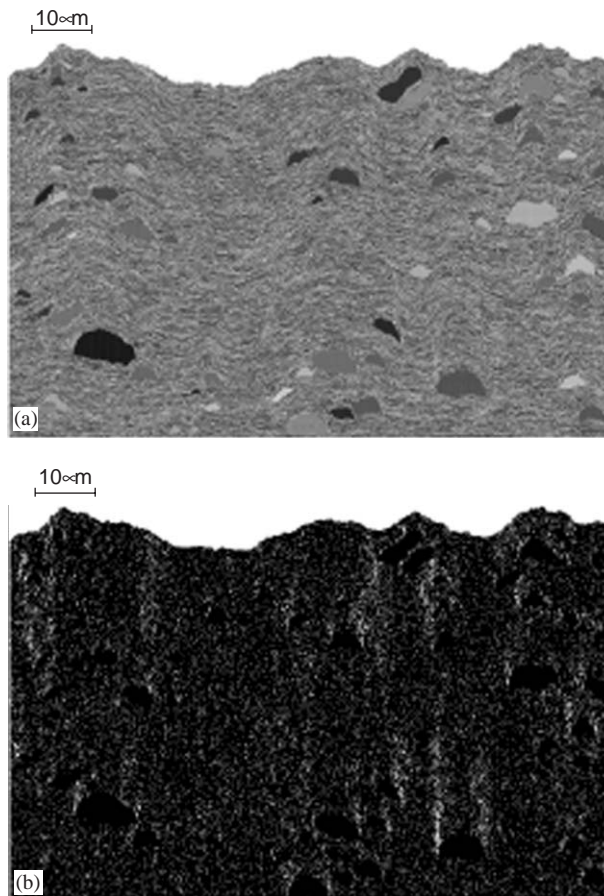

Fig. 18. Simulated (a) microstructure, and (b) pore distribution in the coatings made of particles of nonuniform molten states, which are deposited under the conditions in case 4.

to be attached to the previous deposited coating instead of being bounced off (compare Figs. 17(a) and 18(a)). A comparison of simulation results with experimental studies (e.g., Hanson and Settles, 2003) show that the porosity predicted by the model is higher than the experimentally measured value under similar operating conditions. A possible reason is that the CFD model underpredicts particle temperature due to ignorance of exothermic particle oxidation (Dolatabadi et al., 2003) and contribution of viscous dissipation to the two-phase heat transfer coefficient (Rosner, 2000). However, the relationship between particle temperature (or melting ratio) and porosity as well as deposition efficiency is qualitatively predicted, i.e., increased temperature softens the sprayed particles, thus leading to decreased porosity and increased deposition efficiency. An important finding of this work is that the particles are not necessarily to be fully melted to achieve excellent coating microstructure (see Fig. 18). This is very important for the fabrication of nanostructured coatings, since the nanostructure in the unmelted particles is preserved during flight.

6. Conclusions

A multi-scale modeling framework for the HVOF thermal spray process is developed and applied to the processing of WC–12%Co particles by the Diamond Jet hybrid HVOF thermal spray gun. A particle laden supersonic reacting flow with overexpanded flow condition at the exit of the nozzle is solved using CFD simulation and the formation of coating microstructure is captured by rule-based stochastic simulation. The main findings of this work are summarized below:

1. Particles of moderate sizes achieve higher velocity and temperature at impact than both larger and smaller ones. Particles of sub-micron size may not stick on the substrate due to small momentum inertias.
2. Particle injection velocity has a negligible effect on both particle velocity and temperature (or melting degree).
3. The spray distance has a significant influence on both velocity and temperature (or melting degree) of small particles with size less than 30 μm.
4. The fuel/oxygen ratio plays a very important role in particle heating. An equivalence ratio close to 1.2 for the

propylene/oxygen/air system helps to maximize flame temperature and two-phase heat transfer.

5. A high total gas flow rate helps to maintain of gas velocity and temperature in the free jet at high levels for a longer distance, which leads to enhanced momentum transfer and heat transfer between the gas phase and the particles.

6. The carrier flow rate should be kept to a minimum in order to enhance heat transfer, providing that particles can be fed into the gun smoothly.

7. Particles are not necessarily to be fully melted to achieve low coating porosity and high deposition efficiency.

Since coating microstructure is shown to be sensitive to particle state at the point of impact, precise control of the process parameters to suppress coating variability is necessary for the optimal operation of the HVOF thermal spray process. The reader may refer to (Li et al., 2004 a–d) for results on control of HVOF thermal spray processes as well as to (Christofides, 2002; Chiu and Christofides, 1999, 2000; El-Farra et al., 2001; Kalani and Christofides, 1999, 2000, 2002) for further results on control of particulate processes using population balances.

Notation

A	area of the splat, m^2
A_p	projected area of a particle on the plane perpendicular to the flow, m^2
A'_p	surface area of particles, m^2
Bi	Biot number
c_p	heat capacity at constant pressure, J/mol K for gas or J/kg K for particle
C_D	drag coefficient
$C_{1\varepsilon}, C_{2\varepsilon}, C_\mu$	factors in the turbulence model
d_p	particle diameter, m
D	diameter of the gun barrel, m
E	total energy per unit mass, m^2/s^2
f_p	melting degree of particles
G_k	generation of turbulence kinetic energy due to mean velocity gradients, $kg/m\,s^2$
h	heat transfer coefficient, $W/m^2\,K$
H	enthalpy, J/kg
J	heat transfer rate, W
L_d	average distance between particles, m
k	turbulence kinetic energy, m^2/s^2
K_1, K_2	factors used in Eq. (14)
m	mass, kg
M	mach number
N	total number of species
Nu	Nusselt number
p	pressure, Pa
Pr	Prandtl number
R	gas constant, 8.314 J/mol K
R_i	reaction rate, $kg/m^3\,s$
Re	Reynolds number
S	deformation tensor, 1/s
S_h	source term of heat transfer, W
S_{ij}	mean strain rate, 1/s
T	temperature, K
t	time, s
v	velocity, m/s
We	Weber number
x	coordinate, m
Y_M	contribution of the fluctuating dilatation in compressible turbulence to the overall dissipation rate, $kg/m\,s^3$

Greek letters

α	inverse effective Prandtl number
δ_{ij}	Kronecker delta
ε	turbulence dissipation rate, m^2/s^3
γ	adiabatic constant, ratio of heat capacity at constant pressure to the one at constant volume
λ	thermal conductivity, $J/m^2\,K$
κ	ratio of particle loading to particle/gas density ratio
μ	viscosity, Pa s
μ_{LN}	mean in the lognormal distribution function
ν	kinematic viscosity, m^2/s
ϕ	sphericity, defined as the ratio of the surface area of a sphere with equivalent volume to the actual surface area of a particle
ρ	density, kg/m^3
σ	Stephan–Boltzmann constant, $5.67 \times 10^{-8}\,W/m^2\,K^4$
σ_{LN}	standard deviation in the lognormal distribution function
σ_p	surface tension, kg/s^2
φ	equivalence ratio
ε	emissivity
ε_p	thermal diffusivity of solidified layer, m^2/s
ξ	flattening ratio
ξ_i	stoichiometric coefficient, mol/kg

Subscripts

0	initial value
a	ambient condition
e	exit condition
eff	effective property
g	properties related to gas
i, j, l	indices
m	melting
max	maximum
p	properties related to particles

pr   products
T total
t turbulent
$^{-}$ normalized variable
$\cdot$ time derivative

Acknowledgements

References

Ajdelsztajn, L., Lee, J., Chung, K., Bastian, F.L., Lavernia, E.J., 2002. Synthesis and nanoindentation study of high-velocity oxygen fuel thermal-sprayed nanocrystalline and near-nanocrystalline Ni coatings. Metallurgical and Materials Transactions A 33, 647–655.

Chang, C.H., Moore, R.L., 1995. Numerical simulation of gas and particle flow in a high-velocity oxygen-fuel (HVOF) torch. Journal of Thermal Spray Technology 4, 358–366.

Cheng, D., Xu, Q., Trapaga, G., Lavernia, E.J., 2001a. The effect of particle size and morphology on the in-flight behavior of particles during high-velocity oxyfuel thermal spraying. Metallurgical and Materials Transactions B 32, 525–535.

Cheng, D., Xu, Q., Trapaga, G., Lavernia, E.J., 2001b. A numerical study of high-velocity oxygen fuel thermal spraying process. part I: Gas phase dynamics. Metallurgical and Materials Transactions A 32, 1609–1620.

Cheng, D., Trapaga, G., McKelliget, J.W., Lavernia, E.J., 2003. Mathematical modelling of high velocity oxygen fuel thermal spraying of nanocrystalline materials: an overview. Modelling and Simulation in Materials Science and Engineering 11, R1–R31.

Chiu, T., Christofides, P.D., 1999. Nonlinear control of particulate processes. A.I.Ch.E. Journal 45, 1279–1297.

Chiu, T., Christofides, P.D., 2000. Robust control of particulate processes using uncertain population balances. A.I.Ch.E. Journal 46, 266–280.

Christofides, P.D., 2002. Model-Based Control of Particulate Processes, Particle Technology Series. Kluwer Academic Publishers, Netherlands.

Crowe, C.T., Sommerfeld, M., Tsuji, Y., 1997. Multiphase Flows with Droplets and Particles. CRC Press, Boca Raton, FL, USA.

Dolatabadi, A., Mostaghimi, J., Pershin, V., 2003. Effect of a cylindrical shroud on particle conditions in high velocity oxy-fuel spray process. Journal of Materials Processing Technology 137, 214–224.

El-Farra, N.H., Chiu, T., Christofides, P.D., 2001. Analysis and control of particulate processes with input constraints. A.I.Ch.E. Journal 47, 1849–1865.

Ganser, G.H., 1993. A rational approach to drag prediction of spherical and nonspherical particles. Powder Technology 77, 143–152.

Gil, L., Staia, M.H., 2002. Influence of HVOF parameters on the corrosion resistance of NiWCrBSi coatings. Thin Solid Films 420–421, 446–454.

Gourlaouen, V., Verna, E., Beaubien, P., 2000. Influence of flame parameters on stainless steel coatings properties. In: Berndt, C.C. (Ed.), Thermal Spray: Surface Engineering Via Applied Research, Proceedings of the International Thermal Spray Conference, Montreal, QC, Canada. pp. 487–493.

Gordon, S., McBride, B.J., 1994. Computer program for calculation of complex chemical equilibrium compositions and applications. NASA Reference Publication 1311, Lewis Research Center, Cleveland, OH, USA.

Gu, S., Eastwick, C.N., Simmons, K.A., McCartney, D.G., 2001. Computational fluid dynamic modeling of gas flow characteristics in a high-velocity oxy-fuel thermal spray system. Journal of Thermal Spray Technology 10, 461–469.

Haller, K.K., Ventikos, Y., Poulikakos, D., Monkewitz, P., 2002. Computational study of high-speed liquid droplet impact. Journal of Applied Physics 92, 2821–2828.

Haller, K.K., Ventikos, Y., Poulikakos, D., 2003. Wave structure in the contact line region during high speed droplet impact on a surface: Solution of the riemann problem for the stiffened gas equation of state. Journal of Applied Physics 93, 3090–3097.

Hanson, T.C., Settles, G.S., 2003. Particle temperature and velocity effects on the porosity and oxidation of an hvof corrosion-control coating. Journal of Thermal Spray Technology 12, 403–415.

Hassan, B., Lopez, A.R., Oberkampf, W.L., 1998. Computational analysis of a three-dimensional high-velocity oxygen fuel (HVOF) thermal spray torch. Journal of Thermal Spray Technology 7, 71–77.

He, J.H., Ice, M., Dallek, S., Lavernia, E.J., 2000. Synthesis of nanostructured WC–12 pct Co coating using mechanical milling and high velocity oxygen fuel thermal spraying. Metallurgical and Materials Transactions A 31, 541–553.

Hearley, J.A., Little, J.A., Sturgeon, A.J., 2000. The effect of spray parameters on the properties of high velocity oxy-fuel NiAl intermetallic coatings. Surface and Coating Technology 123, 210–218.

Kalani, A., Christofides, P.D., 1999. Nonlinear control of spatially-inhomogeneous aerosol processes. Chemical Engineering Science 54, 2669–2678.

Kalani, A., Christofides, P.D., 2000. Modelling and control of a titania aerosol reactor. Aerosol Science & Technology 32, 369–391.

Kalani, A., Christofides, P.D., 2002. Simulation, estimation and control of size distribution in aerosol processes with simultaneous reaction, nucleation, condensation and coagulation. Computers & Chemical Engineering 26, 1153–1169.

Lau, M.L., Jiang, H.G., Nuchter, W., Lavernia, E.J., 1998. Thermal spraying of nanocrystalline Ni coatings. Physica Status Solidi A - Applied Research 166, 257–268.

Li, M., Christofides, P.D., 2003. Modeling and analysis of HVOF thermal spray process accounting for powder size distribution. Chemical Engineering Science 58, 849–857.

Li, M., Christofides, P.D., 2004a. Feedback control of HVOF thermal spray process accounting for powder size distribution. Journal of Thermal Spray Technology 13, 108–120.

Li, M., Shi, D., Christofides, P.D., 2004b. Diamond jet hybrid HVOF thermal spray: Gas-phase and particle behavior modeling and feedback control design. Industrial & Engineering Chemistry Research 43, 3632–3652.

Li, M., Shi, D., Christofides, P.D., 2004c. Modeling and control of HVOF thermal spray processing of WC-Co coatings. Powder Technology in press.

Li, M., Shi, D., Christofides, P.D., 2004d. Model-based estimation and control of particle velocity and melting in HVOF thermal spray. Chemical Engineering Science 59, 5647–5656.

Lih, W.C., Yang, S.H., Su, C.Y., Huang, S.C., Hsu, I.C., Leu, M.S., 2000. Effects of process parameters on molten particle speed and surface temperature and the properties of HVOF CrC/NiCr coatings. Surface and Coating Technology 133.

Lopez, A.R., Hassan, B., Oberkampf, W.L., Neiser, R.A., Roemer, T.J., 1998. Computational fluid dynamics analysis of a wire-feed, high-velocity oxygen fuel (HVOF) thermal spray porch. Journal of Thermal Spray Technology 7, 374–382.

Lugscheider, E., Herbst, C., Zhao, L., 1998. Parameter studies on high-velocity oxy-fuel spraying of MCrAlY coatings. Surface and Coating Technology 108–109, 16–23.

Madejski, J., 1976. Solidification of droplets on a cold surface. International Journal of Heat and Mass Transfer 19, 1009–1013.

Mueller, R., Madler, L., Pratsinis, S.E., 2003. Nanoparticle synthesis at high production rates by flame spray pyrolysis. Chemical Engineering Science 58, 1969–1976.

Mueller, R., Jossen, R., Pratsinis, S.E., Watson, M., Akhtar, M.K., 2004. Zirconia nanoparticles made in spray flames at high production rates. Journal of American Ceramic Society 87, 197–202.

Mills, D., 2003. Personal communication, Sulzer Metco.

Oberkampf, W.L., Talpallikar, M., 1996. Analysis of a high-velocity oxygen-fuel (HVOF) thermal spray torch part 2: Computational results. Journal of Thermal Spray Technology 5, 62–68.

Pawlowski, L., 1995. The Science and Engineering of Thermal Spray Coatings. Wiley, Chichester, England.

Power, G.D., Smith, E.B., Barber, T.J., Chiappetta, L.M., 1991. Analysis of a combustion (HVOF) spray deposition gun. Report 91-8, United Technologies Research Center, East Hartford, CT, USA.

Rosner, D.E., 2000. Transport Processes in Chemically Reacting Flow Systems. Dover Publications, Inc, New York, USA.

Shi, D., Li, M., Christofides, P.D., 2004. Diamond jet hybrid HVOF thermal spray: Rule-based modeling of coating microstructure. Industrial & Engineering Chemistry Research 43, 3653–3665.

Sobolev, V.V., Guilemany, J.M., Garmier, J.C., Calero, J.A., 1994. Modelling of particle movement and thermal behavior during high velocity oxy-fuel spraying. Surface and Coating Technology 63, 181–187.

de Villiers Lovelock, H.L., Richter, P.W., Benson, J.M., Young, P.M., 1998. Parameter study of HP/HVOF deposited WC-Co coatings. Journal of Thermal Spray Technology 7, 97–107.

Wegner, K., Pratsinis, S.E., 2003. Nozzle-quenching process for controlled flame synthesis of titania nanoparticles. A.I.Ch.E. Journal 49, 1667–1675.

Xun, Y.W., Lavernia, E.J., Mohamed, F.A., 2004. Synthesis of nanocrystalline Zn-22 pct Al using cryomilling. Metallurgical and Materials Transactions A 35, 573–581.

Yang, X., Eidelman, S., 1996. Numerical analysis of a high-velocity oxygen-fuel thermal spray system. Journal of Thermal Spray Technology 5, 175–184.

Zhang, D., Harris, S.J., McCartney, D.G., 2003. Microstructure formation and corrosion behaviour in HVOF-sprayed Inconel 625 coatings. Materials Science Engineering A 344, 45–56.